

Review

## Review on the Photocatalyst Coatings of TiO<sub>2</sub>: Fabrication by Mechanical Coating Technique and Its Application

Yun Lu <sup>1,\*</sup>, Sujun Guan <sup>1</sup>, Liang Hao <sup>2</sup> and Hiroyuki Yoshida <sup>3</sup>

<sup>1</sup> Graduate School & Faculty of Engineering, Chiba University, 1-33, Yayoi-cho, Inage-ku, Chiba 263-8522, Japan; E-Mail: guansujun1222@gmail.com

<sup>2</sup> College of Mechanical Engineering, Tianjin University of Science and Technology, No.1038, Dagou Nanlu, Hexi District, Tianjin 300222, China; E-Mail: haoliang@tust.edu.cn

<sup>3</sup> Chiba Industrial Technology Research Institute, 6-13-1, Tendai, Inage-ku, Chiba 263-0016, Japan; E-Mail: h.yshd14@pref.chiba.lg.jp

\* Author to whom correspondence should be addressed; E-Mail: luyun@faculty.chiba-u.jp; Tel.: +81-43-290-3514; Fax: +81-43-290-3039.

Academic Editor: Francesco Di Benedetto

Received: 18 June 2015 / Accepted: 22 July 2015 / Published: 30 July 2015

---

**Abstract:** This review presents the latest results of studies directed at photocatalyst coatings of titanium dioxide (TiO<sub>2</sub>) prepared by mechanical coating technique (MCT) and its application. Compared with traditional coating techniques, MCT is a simple, low cost and useful coating formation process, which is proposed and developed based on mechanical frictional wear and impacts between substrate materials and metal powder particles in the bowl of planetary ball mill. The formation process of the metal coatings in MCT includes four stages: The nucleation by adhesion, the formation and coalescence of discrete islands, formation and thickening of continuous coatings, exfoliation of continuous coatings. Further, two-step MCT was developed based on the MCT concept for preparing composite coatings on alumina (Al<sub>2</sub>O<sub>3</sub>) balls. This review also discusses the influence on the fabrication of photocatalyst coatings after MCT and improvement of its photocatalytic activity: oxidation conditions, coating materials, melt salt treatment. In this review, the oxidation conditions had been studied on the oxidation temperature of 573 K, 673 K, 773 K, 873 K, 973 K, 1173 K and 1273 K, the oxidation time of 0.5 h, 1 h, 3 h, 10 h, 15 h, 20 h, 30 h, 40 h, and 50 h. The photocatalyst coatings showed the highest photocatalytic activity with the oxidation condition of 1073 K for 15 h. The metal powder of Ti, Ni and Cr had been used as the coating materials. The composite metal powder could affect the surface structure and photocatalytic

activity. On the other hand, the melt salt treatment with  $\text{KNO}_3$  is an effective method to form the nano-size structure and enhance photocatalytic activity, especially under visible light.

**Keywords:** MCT; formation process; photocatalyst coating; oxidation condition; coating metal; photocatalytic activity; molten salt treatment

---

## 1. Introduction

In the field of materials science and engineering, the investigation into film materials had been the focus of much attention for a variety of new material properties, such as electrics and electronics, optics, thermotics, magnetic, and mechanics, among others [1]. In recent years, without the development of film materials, it would be very difficult to make any great progress in renewable energy, environment improvement, exploitation of space, and so on [2]. In general, the fabrication techniques for film materials can fall into several categories as shown in Table 1 [3]. From Table 1, it can be seen that the fabrication techniques include physical vapor deposition (PVD), chemical vapor deposition (CVD), liquid absorption coating, thermal spraying and mechanical coating. Many variations of these techniques have been developed to balance advantages and disadvantages of various strategies, also shown in Table 1. In these techniques, PVD and CVD are most widely applied, but they require large and complicated equipment and vacuum conditions, and they have high fabrication costs and encounter difficulty in formation on spherical substrate [4–6]. However, every coating technique has its advantages and limitations to some extent. The features of these coating techniques mean that they have different application fields. Their advantages and limitations are summarized in Table 1 [3]. In order to solve these problems, our group had proposed a novel coating fabrication technique to form the coating materials, named as mechanical coating technique (MCT), with the diagram schematic shown in Figure 1 [7,8]. The metal coatings on  $\text{Al}_2\text{O}_3$  balls had been prepared by MCT, shown as Figure 2a, and the metal coatings could be treated by a thermal process, as shown in Figure 2b.

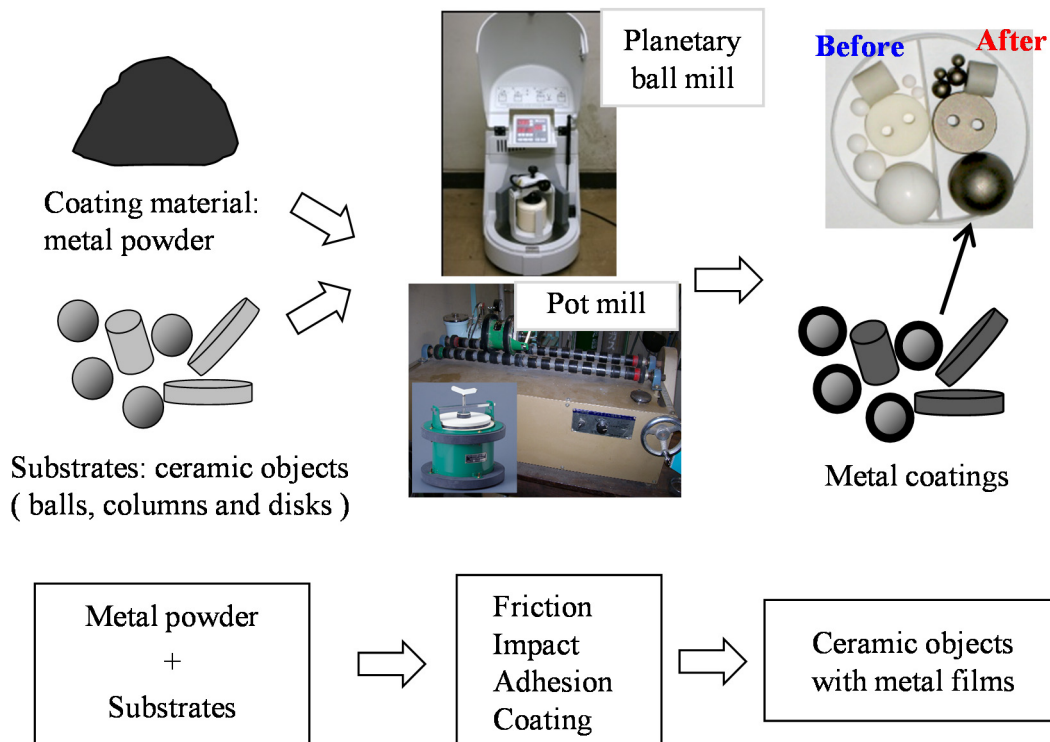
In recent years,  $\text{TiO}_2$  has been considered as one of the most promising photocatalysts for the potential material in environment purification, sterilization, self-cleaning surfaces, and hydrogen generation due to its high photocatalytic activity, excellent chemical stability, non-toxicity, and low cost [9–12]. However, the photoreaction efficiency of  $\text{TiO}_2$  is severely limited to its wider band gap ( $>3$  eV), which hampers the exploitation of solar light in photocatalytic reactions, and in the low quantum efficiency of photocatalytic reactions, because of the high recombination probability of the generated electron-hole pairs [13–15]. Therefore, much effort had been devoted to shifting the absorption of  $\text{TiO}_2$  from UV to visible light range. The ions of transition metal, such as  $\text{Cr}^{3+}$ ,  $\text{V}^{5+}$ ,  $\text{Fe}^{3+}$ ,  $\text{Ni}^{2+}$  are employed to modify the electronic structure of  $\text{TiO}_2$  by introducing a donor and/or acceptor level in the band gap, which allows photons with some lower energy to excite photocatalyst and exhibit a higher photocatalytic activity under visible light [16,17]. On the other hand, the mixed-phase is another way to increase the charge transfer of electrons and holes between the phases of anatase and rutile, which has been paid much attention [18–21]. In our study, MCT had been used to fabricate the  $\text{TiO}_2$  photocatalyst coatings on  $\text{Al}_2\text{O}_3$  balls [22,23]. Collision, friction and abrasion are used to effectively form metal coatings, such Ti, Fe, Zn, and  $\text{TiO}_2$ , on ceramic grinding media [23–25].

**Table 1.** Film coating techniques.

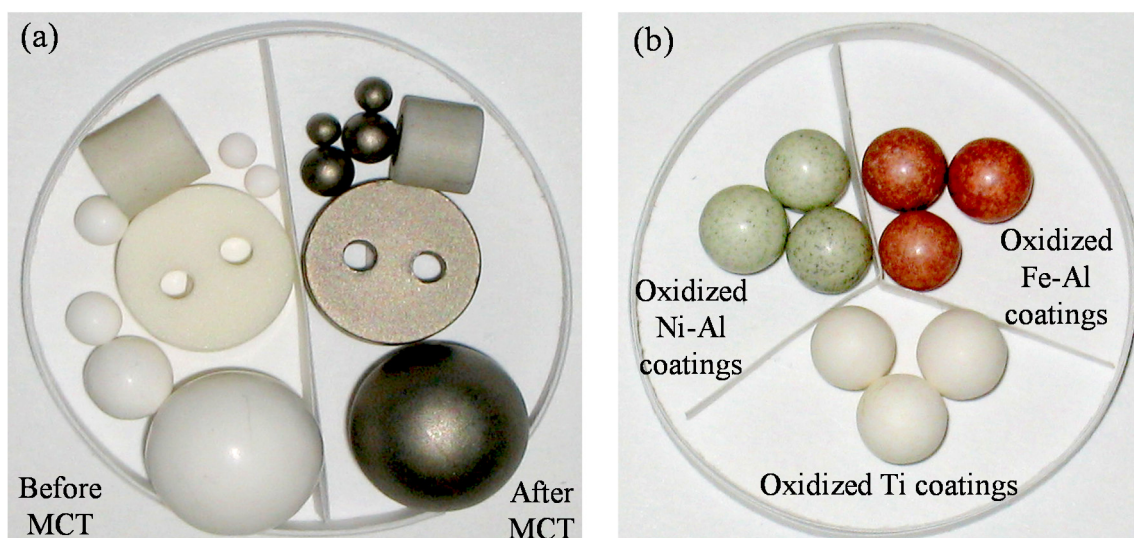
Coating Technique	Coating Processes		Feature	Disadvantage	Application
Physical vapor deposition (PVD)	Vacuum deposition	Resistance heating, Flash Evaporation, Vacuum Arc, Laser heating, High frequency heating, Electron beam heating	Possibility of thickness control; Coating of large area film	Large equipment; Coating difficulty on complicated surface	Chemistry; Optics; Electron
	MBE (Molecular Beam Epitaxy)		Coating on complicated surface; Strong adhesion	Large equipment; Thermal process	Chemistry; Anticorrosive
	Laser deposition		Small equipment; Coating on complicated surface	Solution handling difficulty; Thermal process	Machinery
	Sputter deposition	Ion beam sputtering, DC sputtering, High frequency sputtering, Magnetron sputtering, Microwave ECR plasma deposition	Rapid coating; Large specific surface area	Heat treatment for coating; Crystalline change	Machinery; Automobile; Tool
	Ion beam plating	High frequency ion plating, Activated reactive evaporation, Arc ion plating	Heat treatment needlessness; Possibility of nano-coating	Large equipment; Coating difficulty on complicated surface	Chemistry; Optics; Electron
	Ion beam deposition		Possibility of thickness control; Coating of large area film	Large equipment; Coating difficulty on complicated surface	Chemistry; Anticorrosive
	Ionized cluster beam deposition		Coating on complicated surface; Strong adhesion	Large equipment; Thermal process	Machinery
Chemical vapor deposition (CVD)	Thermal CVD	Atmospheric pressure CVD, Low pressure CVD	Small equipment; Coating on complicated surface	Solution handling difficulty; Thermal process	Machinery; Automobile; Tool
	Plasma CVD	DC plasma CVD, High frequency plasma CVD, ERC plasma CVD	Rapid coating; Large specific surface area	Heat treatment for coating; Crystalline change	Chemistry; Optics; Electron

Table 1. Cont.

Coating Technique	Coating Processes		Feature	Disadvantage	Application
Chemical vapor deposition (CVD)	Photo-excited CVD		Heat treatment needlessness; Possibility of nano-coating	Large equipment; Coating difficulty on complicated surface	Chemistry; Anticorrosive
Liquid absorption coating	Plating	Electroplating, Electroless plating	Possibility of thickness control; Coating of large area film	Large equipment; Coating difficulty on complicated surface	Machinery
	Anodic oxide coating, Painting, Sol-gel method		Coating on complicated surface; Strong adhesion	Large equipment; Thermal process	Machinery; Automobile; Tool
	Spin coating, Dip coating, Roll coating, Spray coating		Small equipment; Coating on complicated surface	Solution handling difficulty; Thermal process	Chemistry; Optics; Electron
Thermal spraying	Flame spraying, Electrical spraying (Arc, Plasma)		Rapid coating; Large specific surface area	Heat treatment for coating; Crystalline change	Chemistry; Anticorrosive
Mechanical coating	Shot coating, Powder impact plating, Aerosol deposition, Gas deposition		Heat treatment needlessness; Possibility of nano-coating	Large equipment; Coating difficulty on complicated surface	Machinery



**Figure 1.** Schematic diagram of fabricating metal coatings by mechanical coating technique (MCT).



**Figure 2.** Appearance of samples by MCT and oxidized metal coatings. (a)  $\text{Al}_2\text{O}_3$  objects before and after MCT; (b) The oxidized metal coatings.

With the subsequent oxidation process, the Ti coatings are oxidized to form  $\text{TiO}_2$  coatings or  $\text{TiO}_2/\text{Ti}$  composite coatings, shown as Figure 2 [26]. The improvement of photocatalytic activity of  $\text{TiO}_2$  coatings via the ions of transition metal and/or the mixed-phase had been studied in detail [27–29].

In this review, we present the latest results of studies directed at photocatalyst coatings of  $\text{TiO}_2$  prepared by MCT and its application.

## 2. A Novel Coating Technique for Composite Coatings: MCT

### 2.1. Proposal of MCT

MCT is a kind of mechanical alloying (MA), which is a powder processing technique that allows production of homogeneous materials starting from blended elemental powder mixtures [30]. In MCT, metal powder and ceramic grinding mediums (balls, buttons and columns) are used as the coating material and the substrates, respectively. Firstly, they are charged into a bowl made of alumina. The mechanical coating is performed by the planetary ball mill (Type: P6, Fritsch, Germany), shown in Figure 3a. The schematic diagram of its operational principle is shown in Figure 3b. In the process, the bowls rotate around their own axes and rotate the rotating support disk simultaneously. Therefore, centrifugal force is produced. Since the bowls and the rotating support disk rotate in opposite directions, the centrifugal force alternately acts in like and opposite directions, shown by way of the ball motion inside the ball mill (Figure 3b). In this condition, the grinding balls in the bowls run down the inner wall of the bowls, which produce friction effect. Subsequently, the ground material and grinding balls lift off and travel freely through the inner chamber of the bowls and impact the opposing inner wall, which results in impact effect.

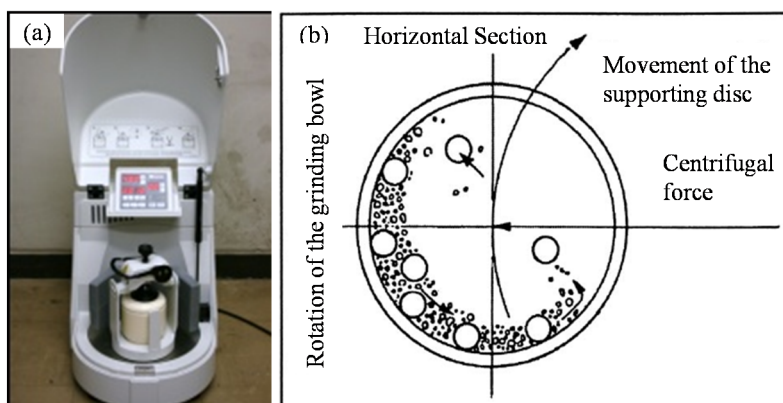


**Figure 3.** Planetary ball mill and ball motion. (a) Planetary ball mill; (b) Schematic depicting the ball motion inside the ball mill.

X-ray diffraction (XRD, JDX-3530, JEOL, Japan) with Cu-K $\alpha$  radiation at 30 kV and 20 mA was used to determine the compositions and crystal structures. The surface morphologies and cross-sectional microstructures of the samples were observed by scanning electron microscopy (SEM) (JSM-5300, JEOL, Tokyo, Japan).

### 2.2. MCT and Its Influencing Parameters

At the early stage of MCT development, we fabricated Ti coatings on ceramic substrates such as Al<sub>2</sub>O<sub>3</sub> balls by MCT. After that, we successfully use other coating materials (Cu, Ni, Fe, Zn, and TiO<sub>2</sub>) to fabricate the coatings by MCT. Figure 4 shows the influence parameters on the coating formation during the MCT, such as the physical factors, chemical factors, process factors and mechanical factors. At present, we focused on the influence parameters of coating materials, electronegativity of metal, plastic deformability of metal, MCT speed and time.

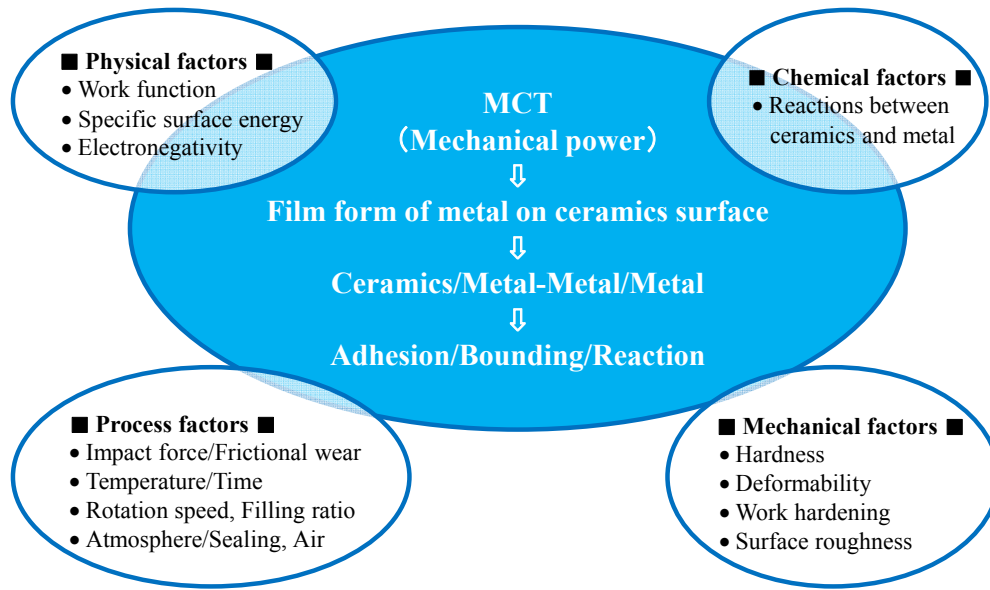


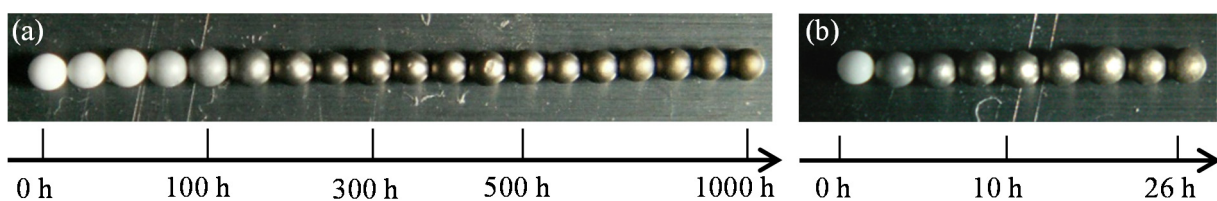
**Figure 4.** The influence parameters of MCT in theory.

2.2.1. Coating Formation by MCT

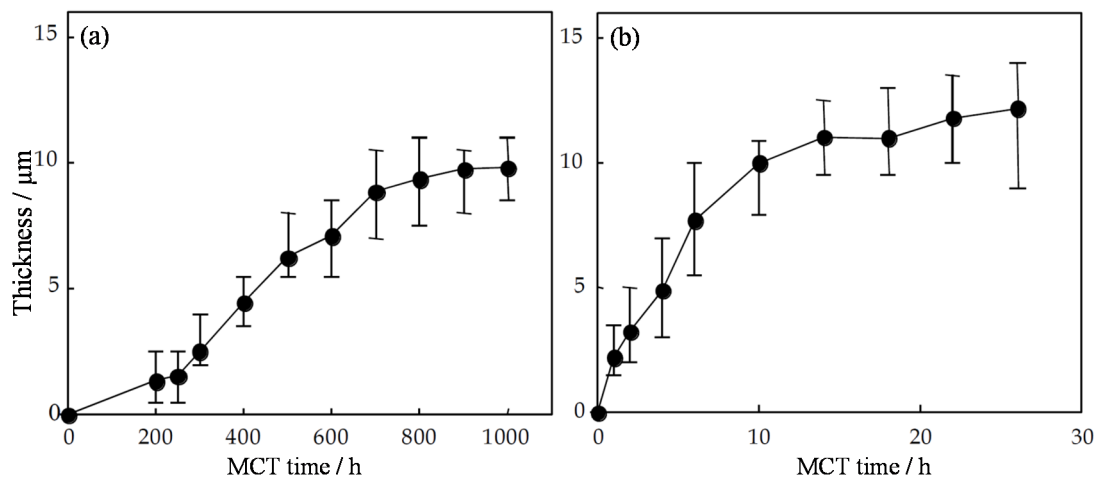
Ti Coatings by MCT

Figure 5 shows the appearances of Ti coatings on Al<sub>2</sub>O<sub>3</sub> balls by MCT, with Ti powder (purity of 99.1%, average diameter of 30 μm) as coating materials, and Al<sub>2</sub>O<sub>3</sub> balls (purity of 93.0%, average diameter of 1 mm) as substrates materials. It can be seen that the color of the Al<sub>2</sub>O<sub>3</sub> balls changed from white to metallic gray, with extended MCT time. That means that more Ti powder particles adhered to the surfaces of the Al<sub>2</sub>O<sub>3</sub> balls. Impact force of only about 1 G can be obtained during MCT performed by pot mill (as shown in Figure 1). When it is carried out by planetary ball mill (as shown in Figure 1), impact force over 10 G or even 40 G can be realized. Therefore, the required MCT time to form Ti coatings can be greatly shortened in the case of the planetary ball mill. With increases in the MCT time, the thickness of Ti coatings increased. The thickness evolution of Ti coatings during MCT was also monitored and is illustrated in Figure 6. Whether a pot mill or planetary ball mill, the coating thickness increased with the increase of MCT time, and they reached 10 and 12 μm, respectively, in pot mill and planetary ball mill after 1000 h and 26 h.

Figure 7 shows SEM images of Ti coatings on Al<sub>2</sub>O<sub>3</sub> balls after MCT, with the MCT set as 300 rpm for 20 h. From Figure 7, it could be seen the Ti coatings had been formed on the Al<sub>2</sub>O<sub>3</sub> balls by MCT, and the thickness of Ti coatings is about 10 μm (Figure 7d).



**Figure 5.** Appearance of Al<sub>2</sub>O<sub>3</sub> balls by MCT. (a) By pot mill; (b) By planetary ball mill MCT.



**Figure 6.** Thickness evolution of Ti coatings with MCT time. (a) By pot mill; (b) By planetary ball mill.

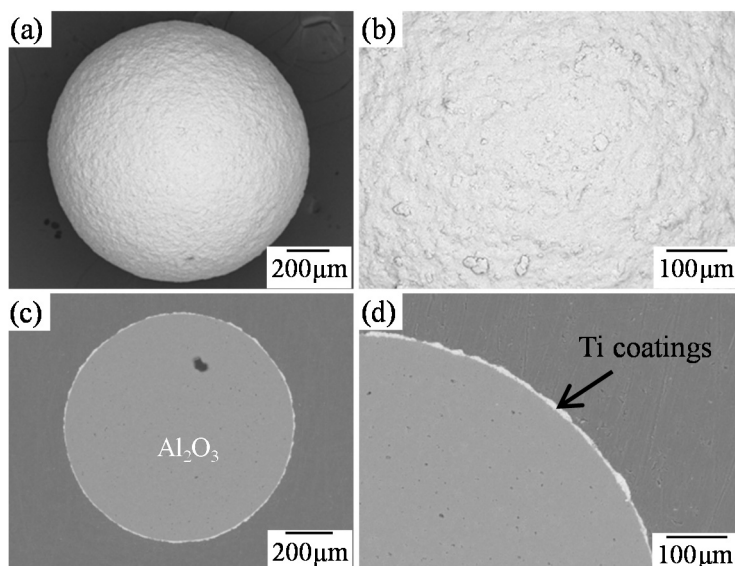


**Figure 7.** Ti coatings by MCT at 300 rpm for 20 h. (a,b) Surface structure; (c,d) Cross sectional structure.

### Coatings by MCT with Other Materials

Based on the Ti coatings fabricated by MCT, other metal coatings had been fabricated, shown as Table 2. Figures 8–11 show SEM images of metal coatings fabricated by MCT. As shown in Figure 8, continuous Cu coatings were prepared on the whole although the surface of Al<sub>2</sub>O<sub>3</sub> balls was not coated with Cu particles at some locations. The thickness of Cu coatings was uniform at about 80 μm.

In Figure 9, only discrete Ni powder particles coated on the surface of Al<sub>2</sub>O<sub>3</sub> balls and continuous Ni coatings were not observed. It could be said that continuous Ni coatings cannot be formed in the present conditions.

As shown in Figure 10, continuous Fe coatings were basically formed on the surface of Al<sub>2</sub>O<sub>3</sub> balls although some surface areas were not coated with Fe particles. The thickness of Fe coatings was confirmed to be about 6 μm.

As shown in Figure 11, continuous Zn coatings were formed, but the surface of Zn coatings was relatively uneven and bulges could be seen. The average thickness was measured to be about 75  $\mu\text{m}$ . According to these results, the preliminary conclusion could be drawn that the coating formation of Cu and Zn is easier to achieve than that of Ni and Fe, with relatively longer MCT time (more than 10 h).

**Table 2.** Source materials' parameters for metal coatings by MCT.

Source Material		Weight (g)	Average Diameter (mm)	Purity (%)
Metal powder	Cu	43.70	0.010	99.8
	Ti	20.00	0.030	99.1
	Ni	10.00	0.005	99.8
	Fe	35.00	0.035	99.5
	Zn	35.00	<0.18	99.8
Ceramic substrate	Al <sub>2</sub> O <sub>3</sub> balls	30.00	1.0	93.0

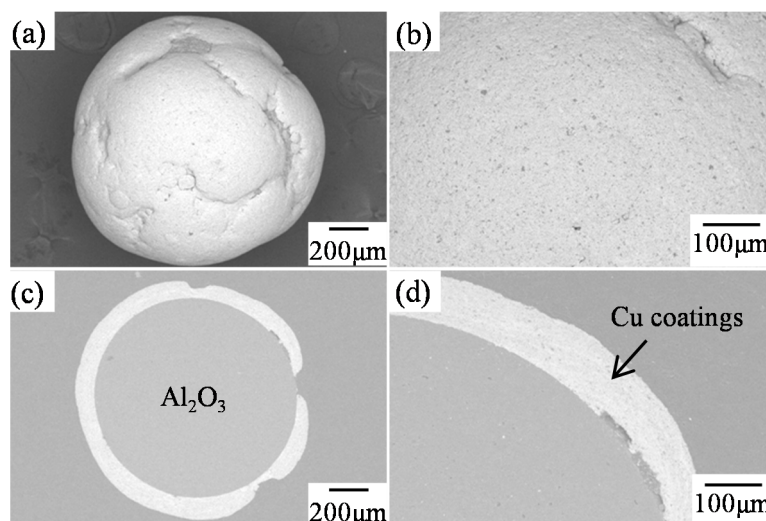


**Figure 8.** Cu coatings by MCT at 480 rpm for 20 h. (a,b) Surface structure; (c,d) Cross sectional structure.

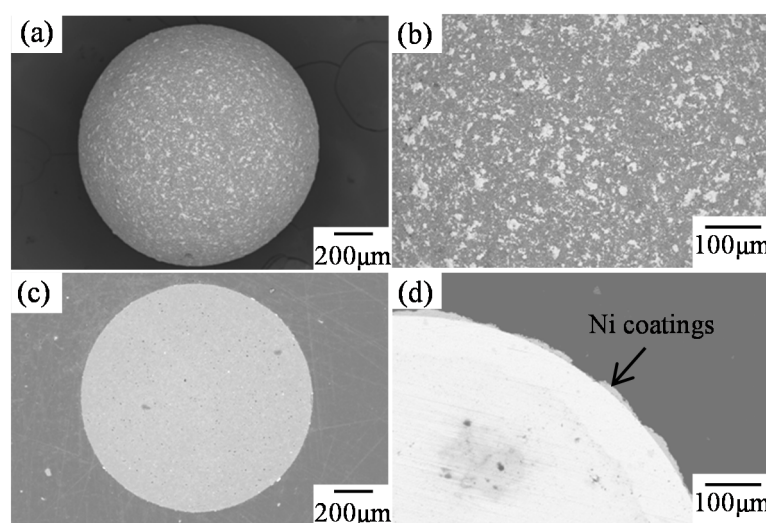


**Figure 9.** Ni coatings by MCT at 480 rpm for 26 h. (a,b) Surface structure; (c,d) Cross sectional structure.

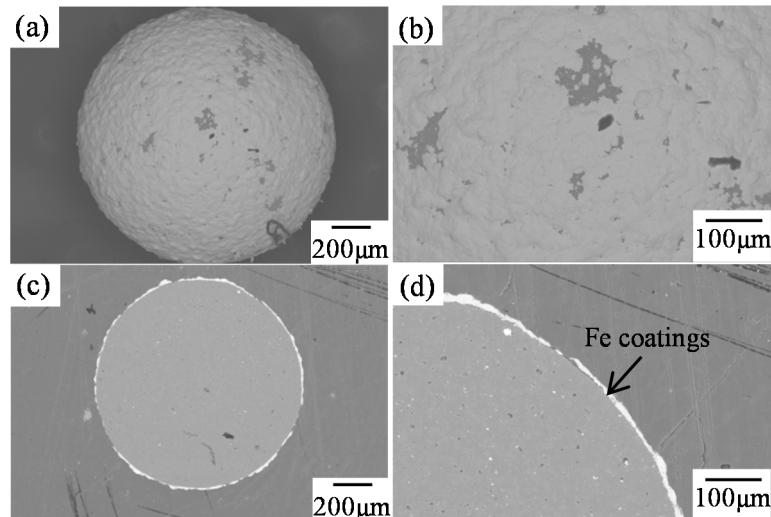


**Figure 10.** Fe coatings by MCT at 300 rpm for 26 h. (a,b) Surface structure; (c,d) Cross sectional structure.

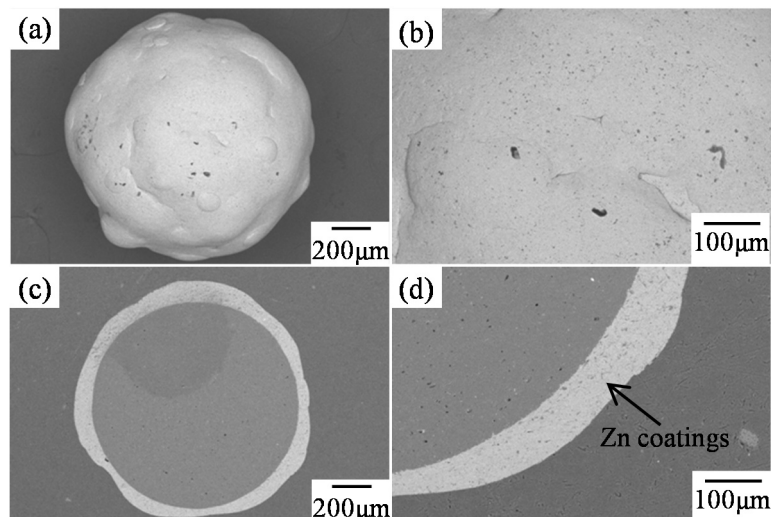


**Figure 11.** Zn coatings by MCT at 300 rpm for 12 h. (a,b) Surface structure; (c,d) Cross sectional structure.

### 2.2.2. Influencing Parameters of MCT

#### Electronegativity of Metal

In order to study the difficulty of coating formation by the different metals (Cu, Ti, Ni, Fe, and Zn), the adhesion of metal particles to the surface of  $\text{Al}_2\text{O}_3$  balls at the initial stage of ball milling was investigated, by MCT at 300 rpm for 2 h, shown as Figure 12. The areas of light and dark colors correspond to metal and alumina, respectively. It can be clearly found that relatively fewer Cu and Ni particles adhered to the surfaces of  $\text{Al}_2\text{O}_3$  balls compared with Ti, Fe, and Zn particles. The coverage of  $\text{Al}_2\text{O}_3$  ball with metal was used to evaluate the adhesion difficulty of tiny metal particles to the surface of  $\text{Al}_2\text{O}_3$  ball. The greater the coverage on the surface of  $\text{Al}_2\text{O}_3$  ball, the easier the adhesion of the metal to the  $\text{Al}_2\text{O}_3$  ball.

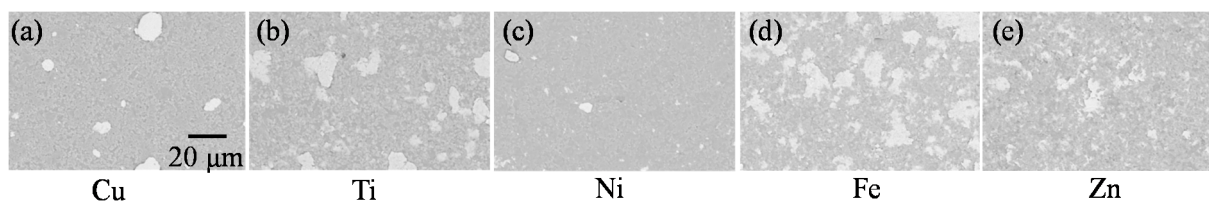


**Figure 12.** Surface SEM images of metal-coated Al<sub>2</sub>O<sub>3</sub> balls by MCT.

Electronegativity is defined as a measure of the ability of an atom in a molecule to attract electrons to itself [31]. The greater the electronegativity (either in Pauling or Allen scale), the easier the atom or the functional group attracts electrons to itself. When metals with a lower electronegativity contact ceramics or polymers, it becomes easier to transfer electrons to the ceramic or polymer. The resulting positive metal cations on the surface coupled with the image charges in Al<sub>2</sub>O<sub>3</sub> produce a surface dipole layer resulting in a greater adhesive strength. This is the main reason why the metal with a lower electronegativity adheres more easily to the surface of the Al<sub>2</sub>O<sub>3</sub> ball. Figure 13 shows the relationship between the initial coverage at 300 rpm for 2 h with metal and the electronegativity of metal. During relatively shorter MCT time (2 h), the coverage of the Al<sub>2</sub>O<sub>3</sub> balls with metals is shown to range from a maximum to a minimum as: Ti > Zn > Fe > Cu > Ni, which is similar to other reports [32,33].

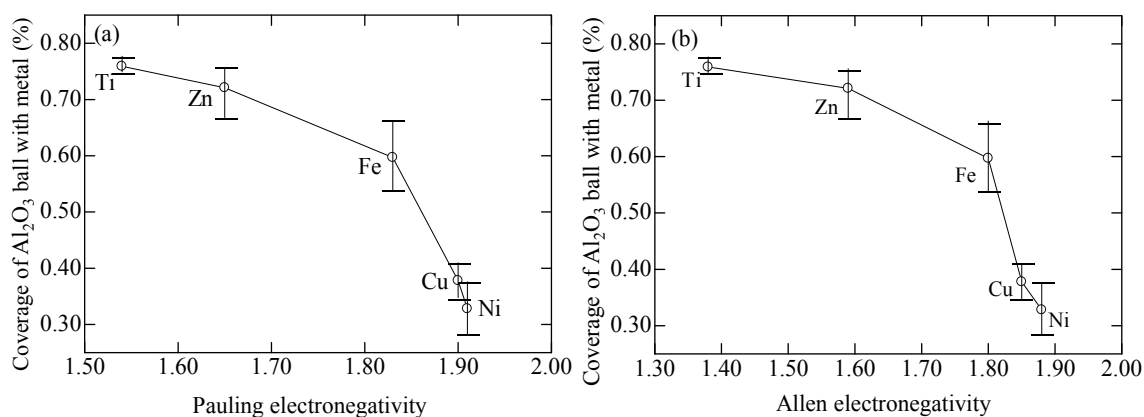


**Figure 13.** Relationship between coverage of Al<sub>2</sub>O<sub>3</sub> ball with metal and electronegativity of the metal. (a) Pauling electronegativity; (b) Allen electronegativity.

### Plastic Deformability of Metal

Generally, yield strength of the metal is used to characterize the plastic deformability of the metal. Metals with lower yield strength show better plastic deformability. Figure 14a shows the maximum average thicknesses of continuous metal coatings as function of the ultimate strength of the annealed metal. It is found that the thickness of continuous metal coatings decreased with an increase in ultimate strength. The order of the thickness varied from maximum to minimum as: Zn > Cu > Ti > Fe. Figure 14b represents the relationship between the maximum average thicknesses of continuous metal coatings and Young's modulus of the annealed metals. The thickness decreased with an increase in Young's modulus except Ti [34]. Therefore, we can conclude that the better the plastic deformability of the metal, the easier was the cold welding among the metal powder particles and the greater the thickness of the continuous metal coatings.

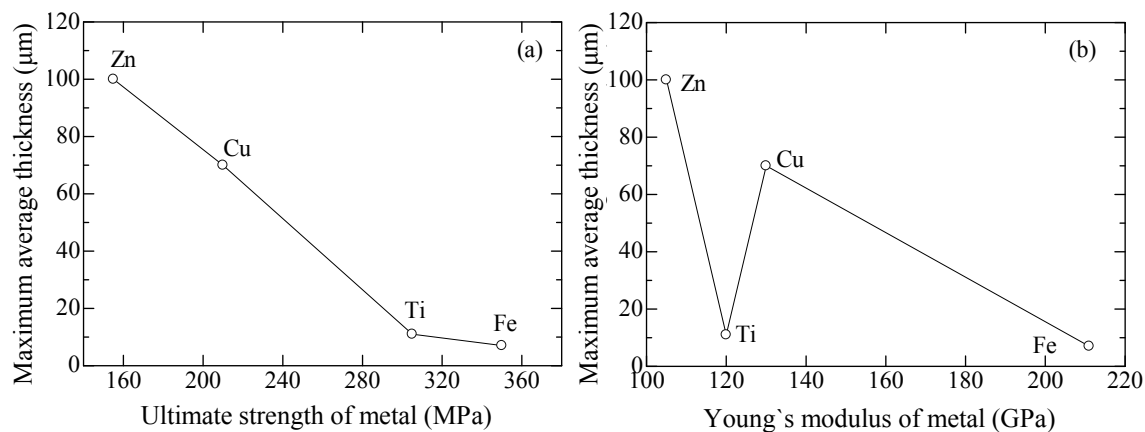


**Figure 14.** Relationship between maximum average thicknesses of continuous metal coatings. (a) Ultimate strength of annealed metals; (b) Young's modulus of annealed metals.

### MCT Speed and Time

In order to study the influence of MCT speed and time on the coating formation during the MCT process, Ti powder was used as the coating material and  $\text{Al}_2\text{O}_3$  balls were used as the substrates. Forty grams of Ti powder and 60 g  $\text{Al}_2\text{O}_3$  balls were charged to an alumina bowl with a volume of 250 mL. A planetary ball mill was employed to perform the mechanical coating operation. The rotation speed of the planetary ball mill (MCT speed) was set from 200 to 480 rpm for a series of milling time (MCT time), as shown in Table 3, with a 10-min milling operation and a following 2-min cooling interval to prevent the bowl from overheating. The prepared samples were labeled as follows. "TA $x$ -y $h$ " is the sample fabricated with Ti powder by MCT at  $x$  rpm for  $y$  hour.

**Table 3.** Experimental conditions for fabricating Ti coatings by MCT.

Sample	MCT Speed, $x$ (rpm)	MCT Time, $y$ (h)	Collision Power ( $\times 10^9 \text{ J}\cdot\text{m}^{-2}\cdot\text{s}^{-1}$ )	$\phi$ (Hz)	Collision Strength ( $\times 10^9 \text{ N}\cdot\text{m}^{-2}\cdot\text{s}^{-1}$ )
TA200-y $h$	200	12, 26, 32, 40, 60	13.59	14.09	61.57
TA300-y $h$	300	4, 8, 12, 16, 20, 26, 32, 40	23.91	21.15	108.50
TA400-y $h$	400	4, 8, 12, 16, 20, 26	35.83	28.21	162.49
TA480-y $h$	480	4, 8, 12, 16	46.33	33.84	210.15

The samples of TA $x$ -y $h$  after MCT show metallic color, shown in Figure 15. At relatively lower MCT speed, the surface is smooth and the speed of coating formation is slow. When increasing the MCT speed, the speed of coating formation accelerated and the surface became uneven, which was caused by higher collision power, frequency and strength, shown in Table 3 [35].

Figure 16 shows the XRD patterns of the samples of TA $x$ -y $h$ . At 200 rpm, the diffraction peaks of Ti are clearly detected after 26 h, while at 480 rpm, the peaks of Ti could be detected only after 4 h. The peaks of  $\text{Al}_2\text{O}_3$  could not be detected after 8 h at 480 rpm, which means the whole surface of  $\text{Al}_2\text{O}_3$  balls had been coated with Ti. The influence of MCT speed on coating formation matches the appearance (color) of samples.

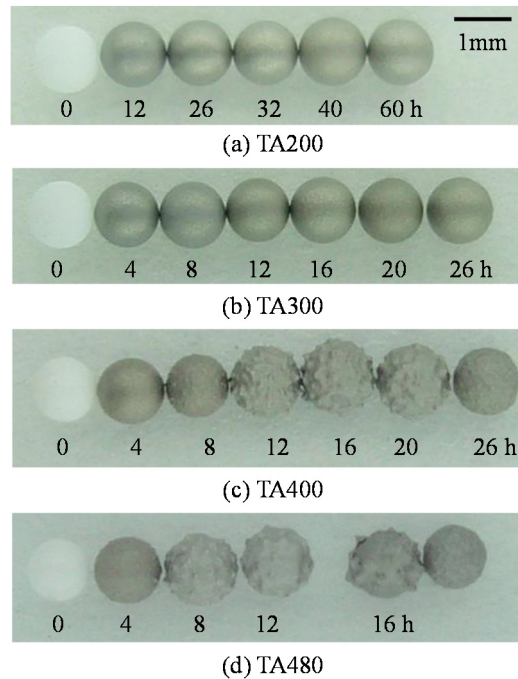


**Figure 15.** Appearance of the samples.

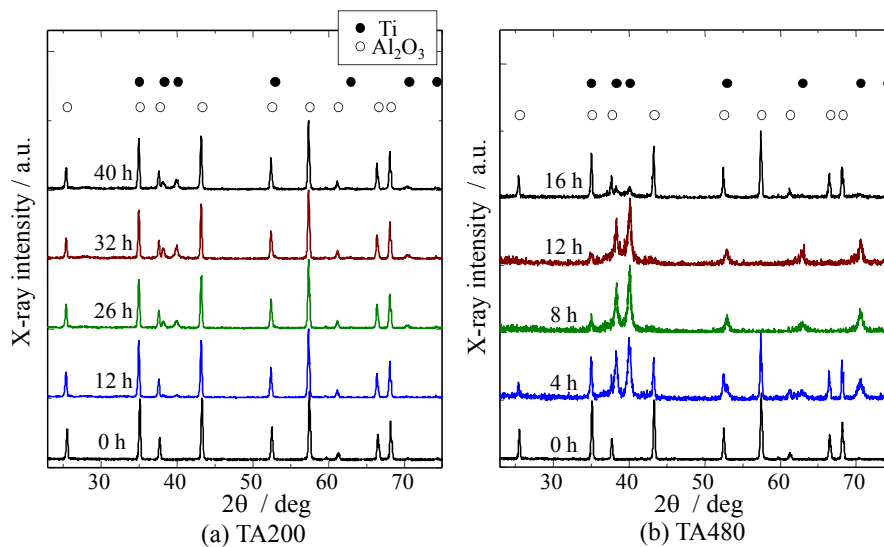


**Figure 16.** XRD patterns of the samples.

The SEM images of TA $x$ -y $h$  samples are shown in Figure 17. When increasing the MCT time, the coatings grew at each MCT speed, which hints that the required time for preparing Ti coatings is shortened, with higher MCT speed by MCT. While at relatively higher speed, the surface of coatings became uneven, and Ti coatings were finally exfoliated from Al<sub>2</sub>O<sub>3</sub> balls when the MCT speed up to 480 rpm for 16 h, shown as Figure 17.

Compared with the cross-sections of samples at different MCT speeds, shown as Figure 18, the Ti coatings became uneven, thickened and formed cracks, even with a shorter time at a relatively higher MCT speed.

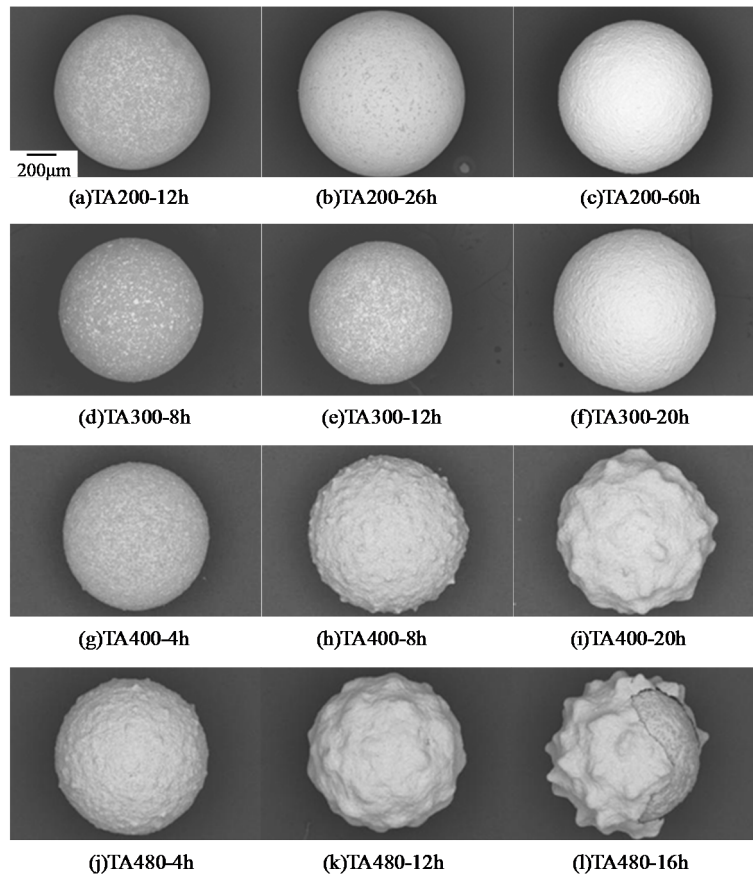


**Figure 17.** SEM images of the surface of the samples.

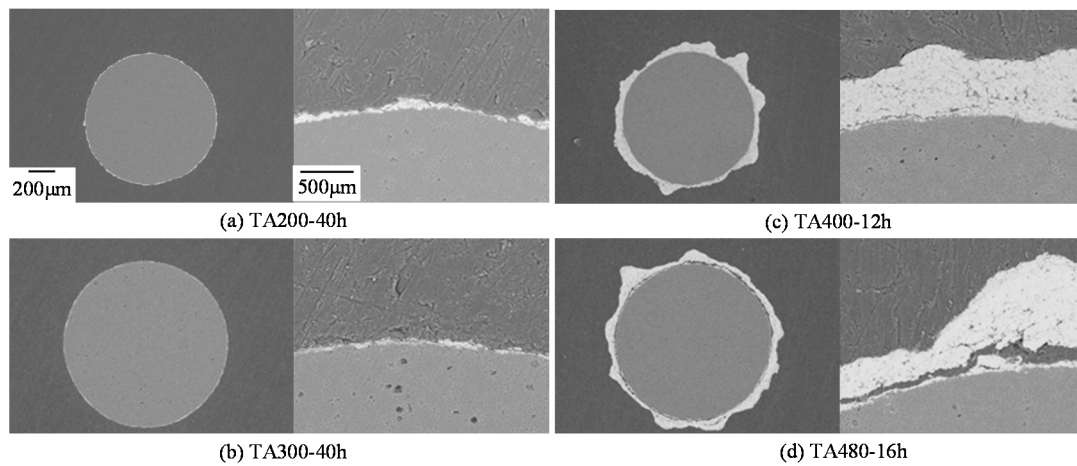


**Figure 18.** SEM images of cross-sectional structure of the samples.

### 2.3. Coating Formation Process of MCT

According to the above results, we summarized the evolution of metal coatings during MCT operation and proposed a model for the evolution. The evolution model of the coating formation process could be summarized according to four stages: nucleation, formation and coalescence of the discrete island, formation of the continuous coatings, and exfoliation, shown as Figure 19 [24].

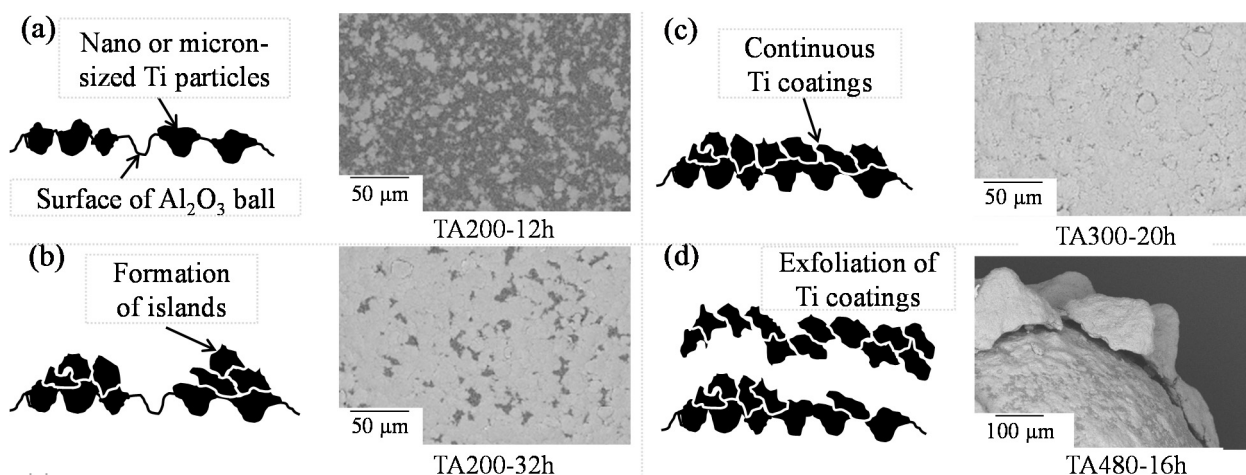


**Figure 19.** Schematic diagram of formation process of surfaces of Ti coatings by MCT.

Based on the coating formation process of MCT, the relationship between the area ratio and the four stages of the coating formation process was given as Figure 20. At the stage of nucleation (I-stage), the surface coverage hardly changes as the nuclei are too small to be detected. When increasing the MCT time, the discrete islands of metal particles are formed, then larger metal particles coat the surface and, hence, the coverage greatly increases (II-stage). When the continuous metal coatings are prepared, the coverage reaches 100% (III-stage). During III-stage, the thickness of coatings is quickly increased. Finally, the coverage is decreased due to the exfoliation of metal coatings (IV-stage).

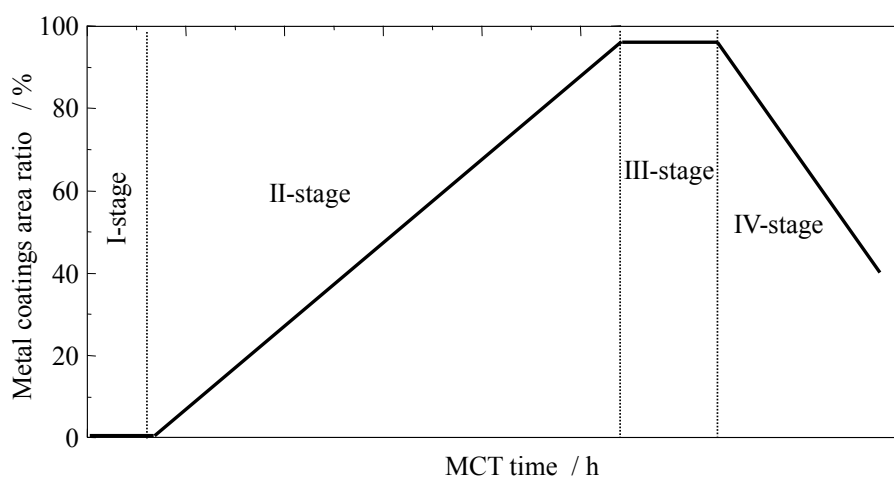


**Figure 20.** Formation process of metal coatings by MCT.

#### 2.4. Two-Step MCT

Based on the MCT, the two-step MCT has been proposed to fabricate the composite photocatalyst coatings of  $\text{TiO}_2/\text{Ti}$ , shown as Figure 21. Firstly, Ti coatings could be fabricated with Ti powder and  $\text{Al}_2\text{O}_3$  balls by MCT, then the Ti coatings on  $\text{Al}_2\text{O}_3$  balls were used as the substrate material and  $\text{TiO}_2$  powder as the coating material. After a certain time milling, the composite photocatalyst coatings of  $\text{TiO}_2/\text{Ti}$  coatings could be fabricated.

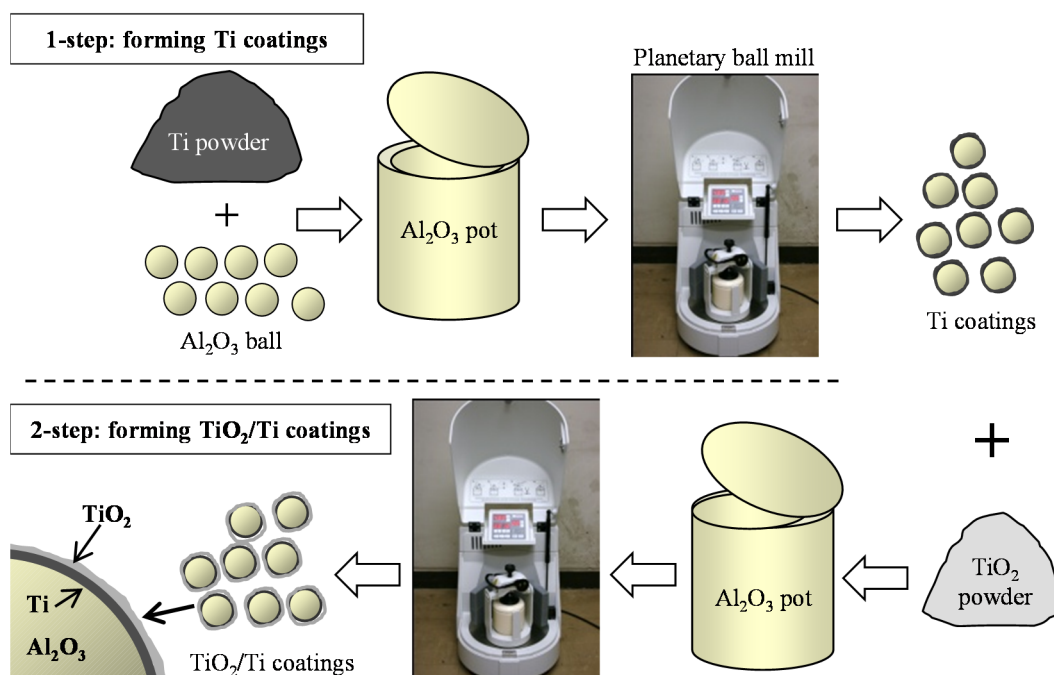


**Figure 21.** Schematic diagram of two-step MCT.

### 3. Application of the Composite Coatings Fabricated by MCT

When discussing the photocatalyst material of TiO<sub>2</sub>, it is well known that this material has been widely used as a photocatalyst. When TiO<sub>2</sub> is used as a photocatalyst, the shape is usually as a film or coating, and fabrication has always been a problem. Regarding the above, our team has developed a new fabrication technique by converse thinking about the powder mixing in mechanical alloying, named as the mechanical coating technique (MCT), and carried out by using coating materials and substrate materials. In general, the photocatalyst coatings of TiO<sub>2</sub> could be fabricated on Al<sub>2</sub>O<sub>3</sub> balls with TiO<sub>2</sub> powder by MCT operation. Due to some factors (the coating formation efficiency, cost and/or size of TiO<sub>2</sub> powder, and so on), at present, our team focused on the oxidation process after MCT to fabricate the photocatalyst coatings, besides the two-step MCT.

In this part, this review presents the studies directed at photocatalyst coatings prepared by MCT and oxidation process, including the influence on photocatalyst coatings by oxidation conditions, adding other metals, and molten slat treatment.

Firstly, here we will introduce the naming method of prepared samples as follows. Regarding the materials as shown as Table 2: “M10-Ti” is the sample fabricated with Ti powder by MCT at 480 rpm for 10 h. “M10-xK-yh” are the final oxidized products of the M10-Ti samples, heat oxidation at the elevated temperature of  $x$  K for  $y$  hour. X-ray diffraction (XRD, JDX-3530, JEOL, Tokyo, Japan) with Cu-K $\alpha$  radiation at 30 kV and 20 mA was used to determine the compositions and crystal structures. The surface morphologies and cross-sectional microstructures of the samples were observed by scanning electron microscopy (SEM) (JSM-5300, JEOL, Tokyo, Japan). The prepared samples firstly dried under UV light (FL20S BLB, Toshiba) for 24 h, then absorbed with 20  $\mu$ mol/L methylene blue (MB) solution under the dark place for 18 h. After these treatments, the photocatalytic activity was evaluated by measuring the degradation rate of 10  $\mu$ mol/L MB solution at room temperature by referring to Japanese industrial standard (JIS R 1703-2: 2007). The diameter of test cell is 18 mm and 40 mm.

The photocatalytic activity test under UV has been reported in detail in our previous work [13]. On the other hand, the photocatalytic activity test under visible light was carried out by the light source of two 20 W fluorescent lamps (NEC FL20SSW/18), which were placed on the top to make sure the samples would obtain 5000 lx. A suitable cut-off filter (L42, Hoya Candeo Optronics Co., Saitama, Japan) was placed to ensure that only visible light ( $\lambda > 420$  nm) could reach the samples. The degradation rate constant  $R$  ( $\text{nmol}\cdot\text{L}^{-1}\cdot\text{h}^{-1}$  and  $\text{nmol}\cdot\text{L}^{-1}\cdot\text{min}^{-1}$  for the test cell of 18 mm and 40 mm, respectively) of MB solution concentration *versus* irradiation time was calculated by the least squares method with the data, by referring to Japanese industrial standard (JIS R 1703-2: 2007). In order to clearly show the photocatalytic activity, here we use the  $R$  value to describe the difference in the degradation rate constants  $k$ .  $R$  is calculated by the equation:

$$R = k - k_{MB} \quad (1)$$

where  $k_{MB}$  is to describe the degradation rate constants of MB solution without samples.

### 3.1. Influence on Photocatalyst Coatings of $\text{TiO}_2$ by Oxidation Condition

During this study, the oxidation conditions focus on temperature and time. According to the Gibbs' free energy theory, the influence on the crystal phase of  $\text{TiO}_2$  by temperature is more direct than that of time, and the crystal phase is one of the most important factors for photocatalytic activity of photocatalyst  $\text{TiO}_2$ . Therefore, we divided this part into oxidation temperature and oxidation time.

#### 3.1.1. Focusing on Oxidation Temperature

Figure 22 shows the appearance photograph of M10- $x$ K- $y$ h samples. The Ti coatings (M10-Ti) show metallic color [8]. In contrast, the M10- $x$ K- $y$ h samples appear to have various colors, under different oxidation conditions, as shown in Figure 22. The color of  $\text{TiO}_2$  is related to the thickness of  $\text{TiO}_2$  coatings if the thickness is nano-sized, which hints the samples of  $\text{TiO}_2$  coatings with different thicknesses and nano-sizes were formed by each oxidation condition [27,36].

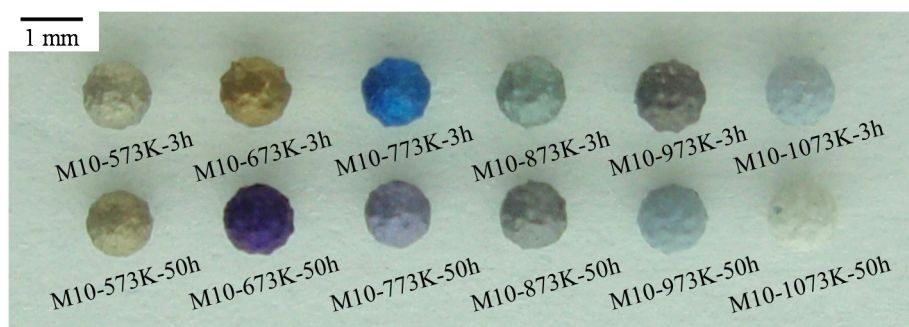


**Figure 22.** The appearance of the samples.

Figure 23 shows the XRD patterns of the photocatalyst coatings on  $\text{Al}_2\text{O}_3$  balls. It can be seen that only the diffraction peaks of Ti are detected for the M10-Ti samples. With the oxidation time of 3 h, the crystal structures of samples changed with the oxidation temperature are (1) anatase phase started to appear at  $38.57^\circ$  from the sample oxidized at 673 K, (2) mixed-phase of anatase and rutile started to appear at 873 K, and (3) anatase started to disappear at 1073 K. While extended the oxidation time to be

50 h, the crystal structures changed with the oxidation temperature are (1) anatase phase appeared at 673 K, (2) mixed-phase appeared at 773 K, and (3) anatase disappeared at 1073 K. As we know, the anatase-rutile phase transformation is a metastable-to-stable transformation and there is no equilibrium transformation temperature [37]. According to the Gibbs' free energy ( $G$ ) for the two phases (anatase, rutile), the energy difference  $\Delta G$  between anatase and rutile phases at 773 K and 873 K are  $3908 \text{ J}\cdot\text{mol}^{-1}$  and  $3353 \text{ J}\cdot\text{mol}^{-1}$ , respectively. Therefore, with extended oxidation time, the temperature of phase transformation had been decreased from 873 to 773 K. For comparison, the mass fraction of rutile ( $X_R$ ) was calculated from the respective peak intensities using the following equation [38]:

$$X_R(\%) = \{1 - (1 + 1.26 I_R/I_A)^{-1}\} \times 100 \quad (2)$$

where  $I_R$  and  $I_A$  are X-ray intensities of the rutile (110) and anatase (004) peaks, respectively. The relationship between  $X_R$  and the oxidation temperature with 3 h and 50 h is shown in Figure 24. The results show that the fraction of rutile ( $X_R$ ) had been increased quickly with extended oxidation time, and the  $X_R$  at 973 K with 50 h is higher than that of 3 h.

SEM images of the surfaces of the samples are shown in Figures 25 and 26. In Figure 25, no reaction compound is not detected from the surfaces of the samples oxidized at temperatures under 773 K with 3 h. A few reaction compounds as point-shape appeared from the samples oxidized at temperatures of 873 K. When increasing the oxidation temperature, the reaction compounds increase in number and finally grow to form the nano-size needle structure. It can be concluded that the observed reaction compounds are the rutile phase of  $\text{TiO}_2$ , according to the needle-like structure and the XRD results above [39].

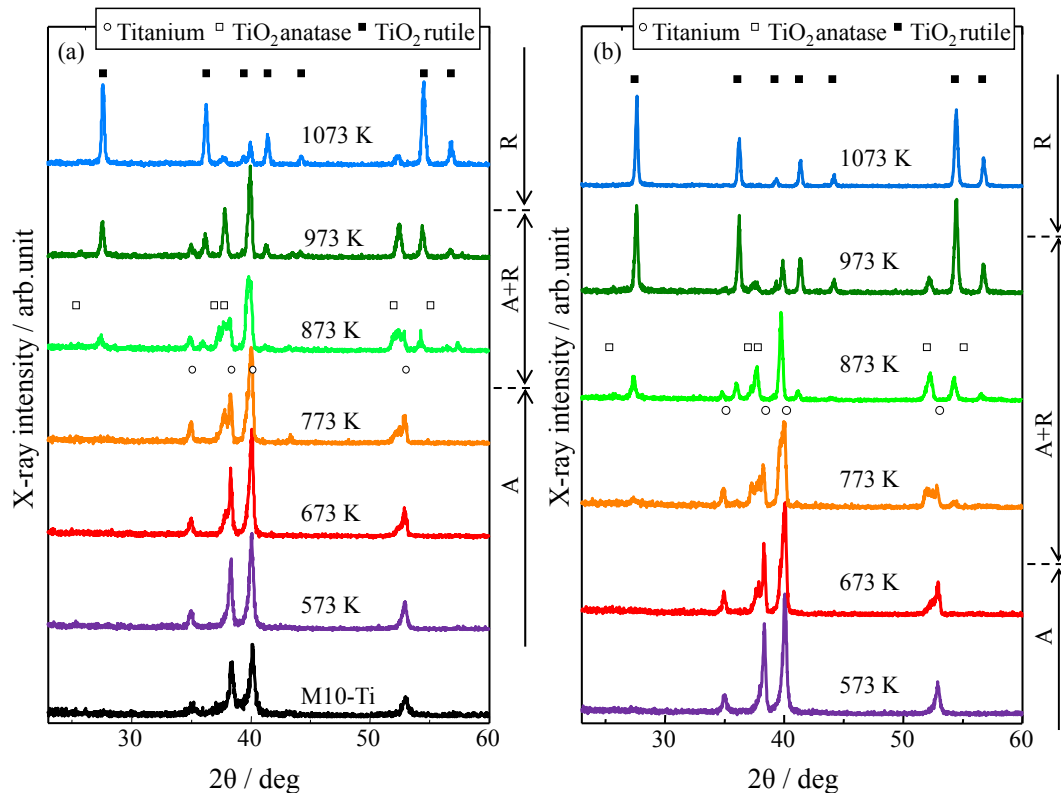


**Figure 23.** XRD patterns of M10-Ti and M10-xK-yh samples. (a) Oxidation time: 3 h; (b) Oxidation time: 50 h.

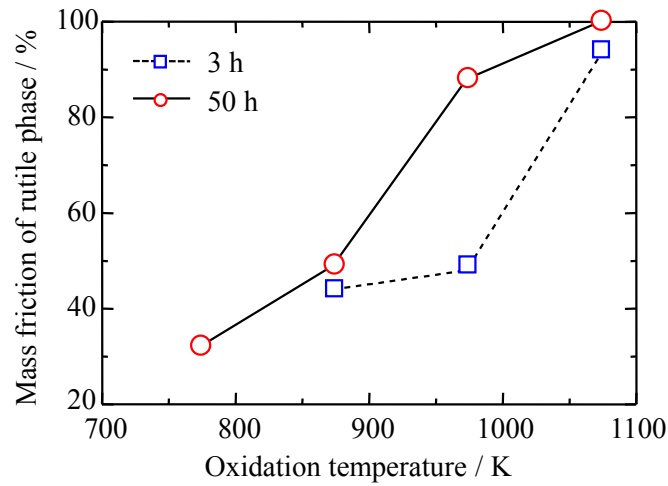


**Figure 24.** Mass fraction of rutile phase of the Ti coatings after oxidation.

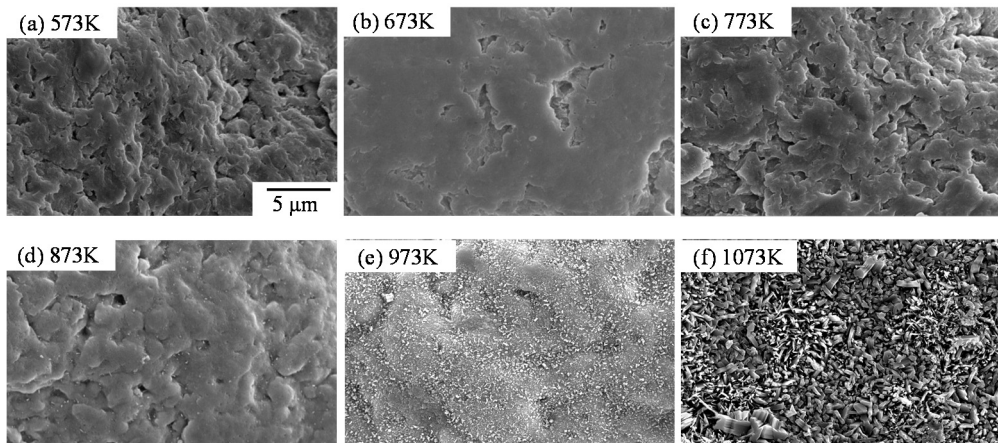


**Figure 25.** SEM images of surfaces of M10-xK-3h samples.

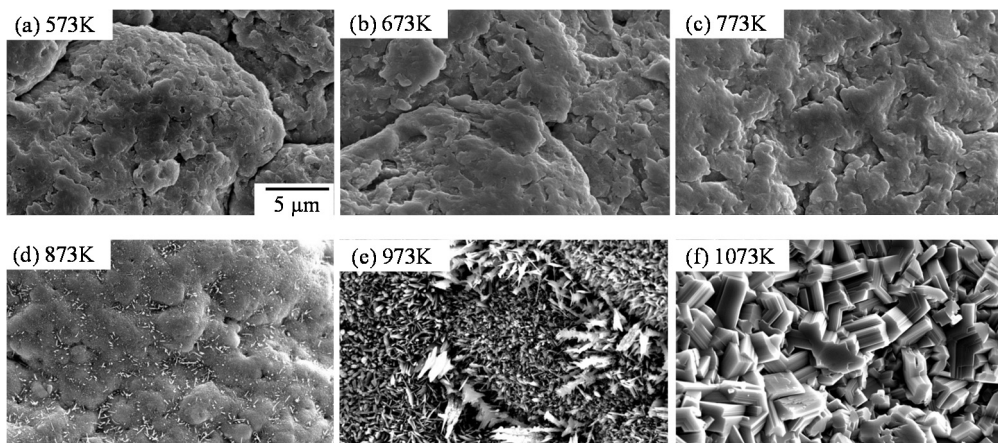


**Figure 26.** SEM images of surfaces of M10-xK-50h samples.

When extending the oxidation time to 50 h (Figure 26), there is also no observed reaction compound, even at 773 K. The reaction compounds also started to be detected from the temperature of 873 K, and the number of the needle-like structures is more than that during 3 h. When the temperature is increased up to 973 K and 1073 K with the oxidation time of 50 h, the structures of nano-size needles grow to

become fiber-like structures (Figure 26e), and finally form columnar-like structures (Figure 26f). These mean the oxidative effect at relatively lower temperatures almost reached that of higher temperatures with an extended oxidation time, which is in line with the known time-temperature equivalence principle [40]: The structure at 873 K of 50 h is similar to that of 973 K of 3 h.

Figures 27 and 28 show SEM images of the cross sections of the samples. The oxidized layer could not be detected from the samples at oxidation condition of 873 K for 3 h and 773 K for 50 h, respectively. If the oxidation temperature was increased up to 973 K during 3 h, the oxidized layer on the coatings could be clearly observed from the outer layer and parts of the inner layer, which forms the  $\text{TiO}_2/\text{Ti-TiO}_2$  structure. When extending the oxidation time to 50 h, the  $\text{TiO}_2/\text{Ti-TiO}_2$  structure could be observed at 873 K, which matches the XRD pattern. With increases in the temperature for the same duration or increasing the duration and maintaining the temperature (higher than 873 K), the oxidized layer increases to become more obvious and thicker, which is in line with the time-temperature equivalence principle. Figure 29 shows the increase in thickness of  $\text{TiO}_2$  coatings is linear, at an oxidation temperature of 1073 K. When the oxidation lasts up to 50 h, the reason for the larger thickness is that Ti coatings were almost oxidized into  $\text{TiO}_2$  coatings, shown as Figure 28f. Therefore, the thickness of  $\text{TiO}_2$  coatings is related with the thickness of the formed Ti coatings during MCT process.

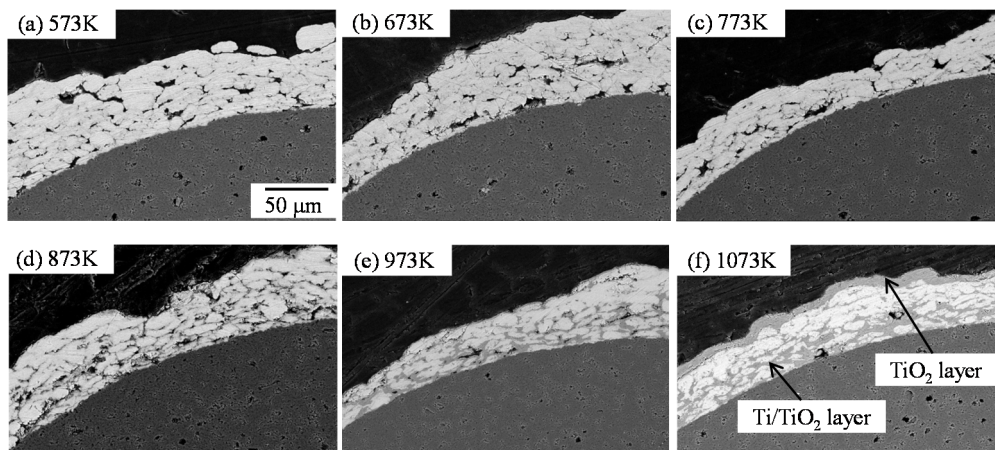


**Figure 27.** SEM images of cross sections of M10-xK-3h samples.

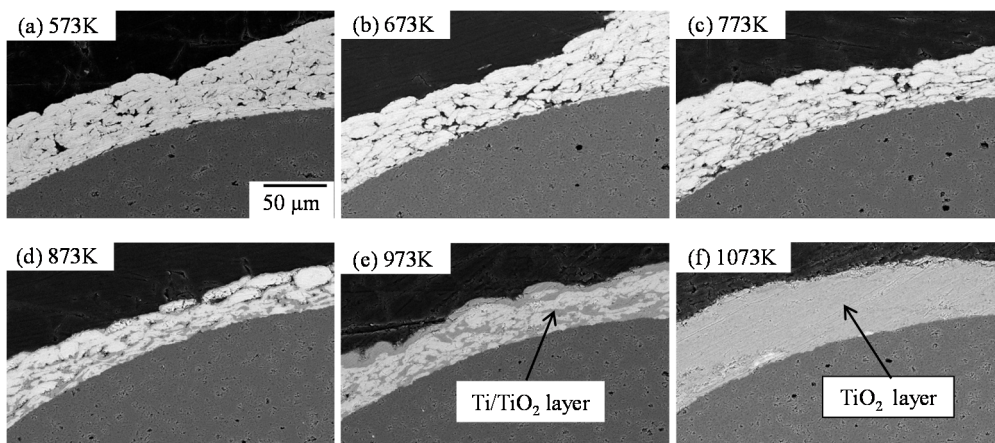


**Figure 28.** SEM images of cross sections of M10-xK-50h samples.

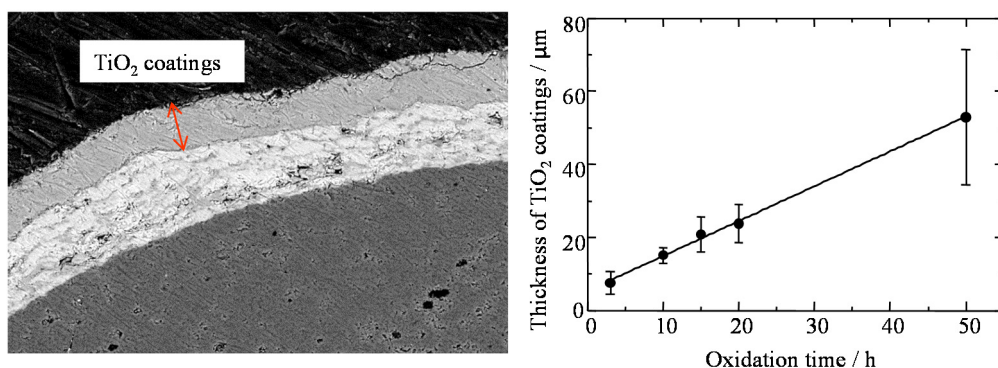


**Figure 29.** Relationship between oxidation time at 1073 K and thickness of TiO<sub>2</sub> coatings.

Figure 30 shows the degradation of MB solution in the presence of the samples under UV irradiation, with the diameter of test cell is 18 mm. The concentration of the blank (marked with MB solution) hardly decreased, which hints the MB solution did not degrade. According to the Ti coatings (marked with M10-Ti), Ti coatings also hardly have any photocatalytic activity. However, the oxidized samples all show the photocatalytic activity, according to the change of concentration of MB solution. The samples oxidized by the temperature of 673 K show higher photocatalytic activity than others, as to the main anatase phase [18]. When increasing the temperature, the anatase phase transformed into rutile phase, and the photocatalytic activity decreased, which suggests that the photocatalytic activity of anatase TiO<sub>2</sub> is higher than that of mixed-phase or rutile TiO<sub>2</sub> under UV irradiation [41–44]. Figure 31 shows the trend of the degradation rate constants  $R$ , calculated from the plots of concentration *versus* irradiation time curves. Presented by the samples oxidized at a series of temperatures with 3 h and 50 h, the trend of  $R$  first increased and then decreased, finally remaining almost constant. In contrast,  $R$  of the samples with the oxidation time of 50 h is higher than that of 3 h, which is below that at temperatures from 573 to 1073 K.

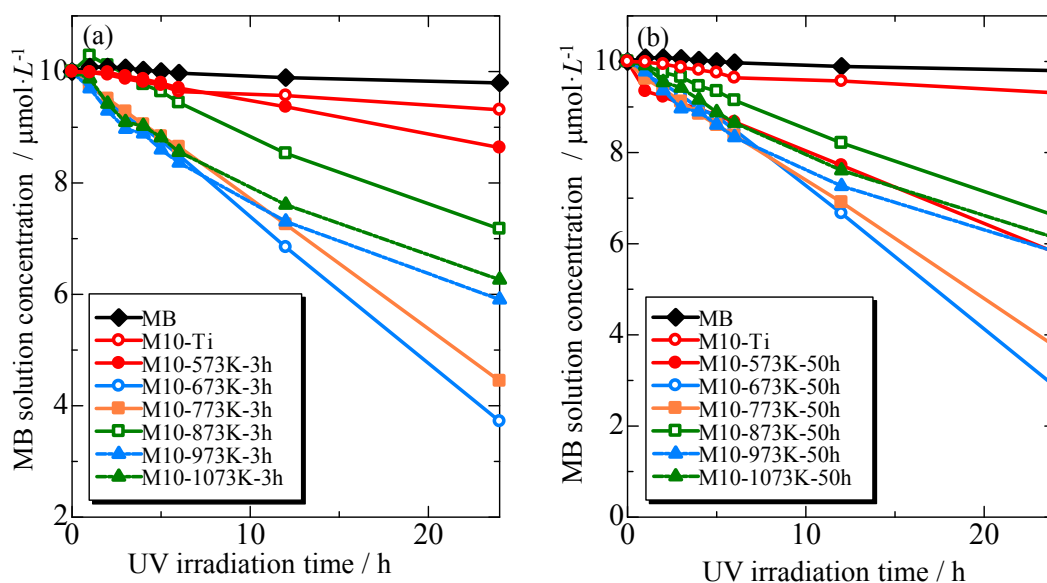


**Figure 30.** Relationship between MB solution concentration and UV irradiation time of samples.

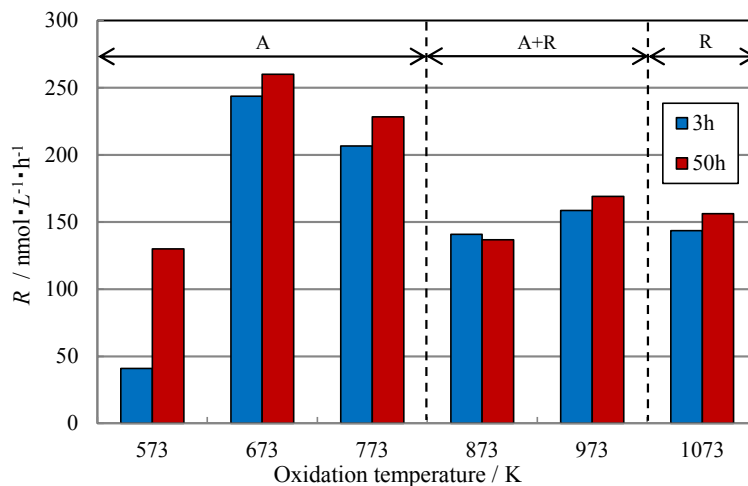


**Figure 31.** Degradation rate constant of M10-xK-yh samples.

The photocatalytic activity of samples might depend on the crystal structure and morphology, which could be controlled by changing the oxidation condition. With the growth of the anatase phase of samples, the photocatalytic activity is the highest at the temperature of 673 K with almost anatase TiO<sub>2</sub>, because anatase is a better photocatalyst than rutile [45]. When increasing the temperature, phase transformation from anatase to rutile would occur. However, at the temperature of 873 K, the content of rutile is little, and the charge transfer between rutile and anatase is limited to some extent [18]. Meanwhile, at temperatures up to 973 K, the photocatalytic activity is higher, because sufficient rutile content had been formed, and the charge transfer between rutile and anatase could suppress the recombination [46–48]. However, photocatalytic activity of the samples oxidized at 1073 K is decreased. That may be related to the extent of rutile formed, as rutile phase absorbs much light. In addition, the microstructures of surface at 973 K are needle-like structures, which is better than that with too little rutile oxidized at 873 K and with too much or larger size rutile at 1073 K. According to the results showing the cross-section and photocatalytic activity, it seems the influence of thicknesses from 8 to 52 μm at 1073 K on photocatalytic activity was not significant.

### 3.1.2. Focusing on Oxidation Time

In order to further investigate the oxidation condition on the photocatalyst coatings of TiO<sub>2</sub>, this part focuses on the oxidation time, at temperatures from 973 to 1273 K.

Figures 32 and 33 show the surface morphologies of the coatings fabricated by the MCT and subsequent heat oxidation at 973 and 1073 K. Figure 32b,c indicates that nano-sized TiO<sub>2</sub> needles formed. With increasing oxidation time, the size of the needles increased and columnar TiO<sub>2</sub> nanocrystals formed (Figure 32d,e). When the oxidation temperature was increased to 1073 K (Figure 33), nano-sized TiO<sub>2</sub> needles grew rapidly and micron-sized columnar TiO<sub>2</sub> crystals formed as the oxidation time was increased. The formation and growth of nano-sized TiO<sub>2</sub> needles and micron-sized columnar TiO<sub>2</sub> crystals have been discussed in many papers [49–51]. It should result from the preferential growth of TiO<sub>2</sub> crystals in a specific direction.

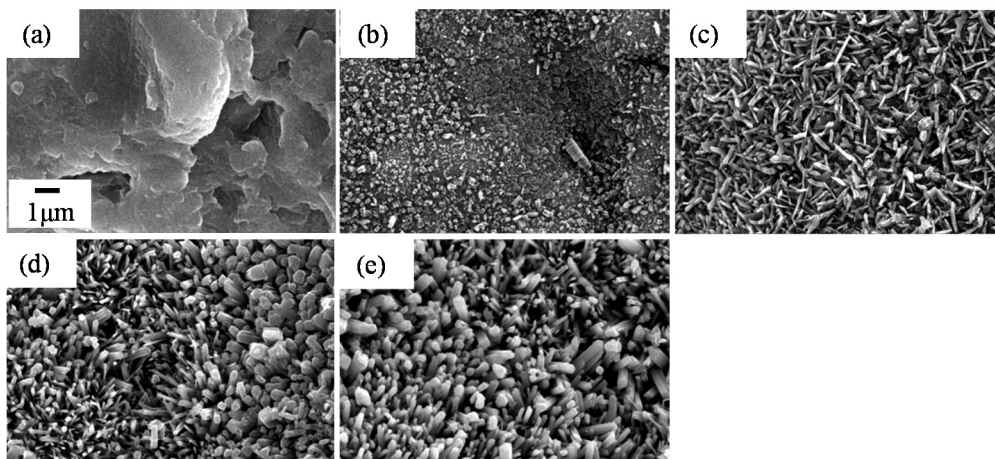


**Figure 32.** SEM images of surfaces of M10-973 K-yh samples. (a) Ti coatings before oxidation, and after oxidation time for (b) 3 h, (c) 10 h, (d) 30 h and (e) 50 h.

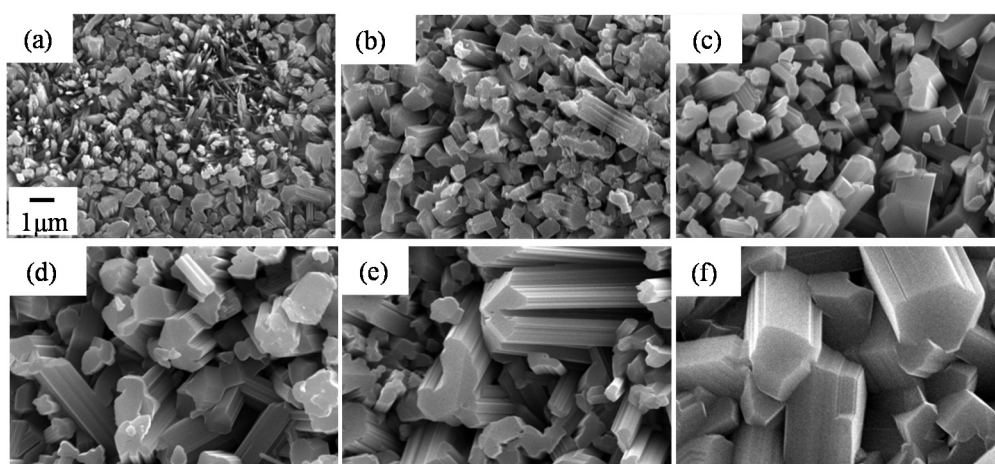


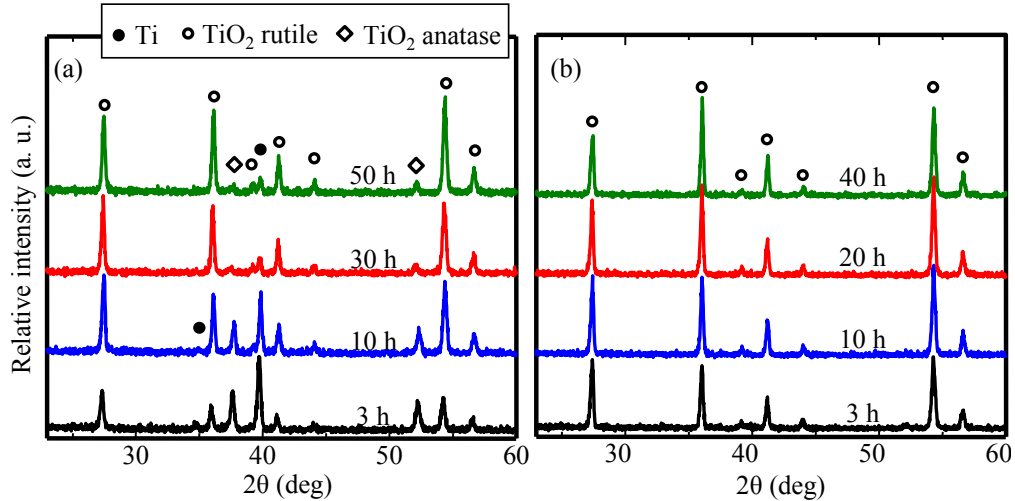
**Figure 33.** SEM images of surfaces of M10-1073 K-yh samples. (a) 3 h, (b) 10 h, (c) 20 h, (d) 30 h, (e) 40 h and (f) 50 h.

The XRD patterns of the Ti coatings oxidized at 973 and 1073 K are shown in Figure 34, respectively. Figure 34a shows the peaks of rutile  $\text{TiO}_2$  became higher while those of Ti and anatase  $\text{TiO}_2$  decreased, with increasing oxidation time. Combined with the results and analysis from Figure 32, the crystal  $\text{TiO}_2$  changes from anatase to rutile, and the surface morphology of  $\text{TiO}_2$  becomes larger—from nano-sized needles to micron-sized columnar

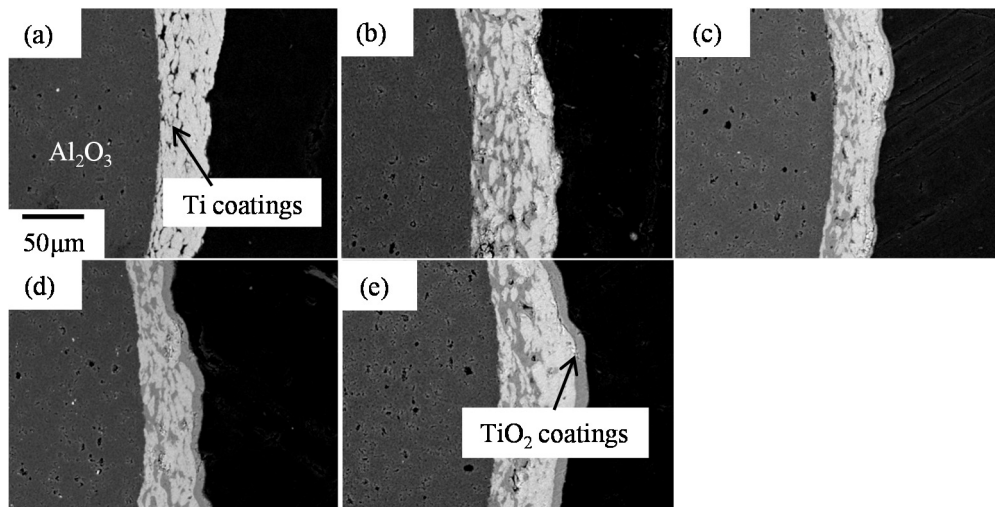
When the oxidation temperature was increased to 1073 K (Figure 34b), the peaks of rutile  $\text{TiO}_2$  were detected while those of Ti coatings were not found. It means that relatively thick rutile  $\text{TiO}_2$  layers formed on the surface of the Ti coatings. The peaks of anatase  $\text{TiO}_2$  were not detected, which indicates that anatase as a metastable phase cannot be formed or has been transferred to rutile at the high temperature. The above results shows that anatase phase can be obtained at 973 K while it cannot be prepared at 1073 K.

Figure 35 shows the cross-sectional SEM images of these coatings fabricated by the MCT and subsequent heat oxidation at 973 K in air for different oxidation times. The light and dark areas of these coatings were confirmed to be Ti and  $\text{TiO}_2$  by XRD analysis, respectively. Figure 35a shows numerous small pores in Ti coatings, which had a thickness of about 50  $\mu\text{m}$ . The inner and surface layers of the Ti

coatings were found to be oxidized simultaneously (Figure 35b–e). It indicates that the coatings were porous and can be penetrated by air. As the oxidation time increased, the thickness of the  $\text{TiO}_2$  layers was increased. From the above analysis, it can be confirmed that  $\text{TiO}_2/\text{Ti}$  composite coatings were prepared after the Ti coatings were oxidized at 973 K.



**Figure 34.** XRD patterns of the of M10-xK-yh samples. (a) 973 K and (b) 1073 K.



**Figure 35.** Cross-section SEM images of M10-973 K-yh samples. (a) before oxidation, (b) 3 h, (c) 10 h, (d) 30 h and (e) 50 h.

The cross-section SEM images of these coatings fabricated by the MCT and subsequent heat oxidation at 1073 and 1173 K are shown in Figures 36 and 37, respectively. Compared with the samples oxidized at 973 K (Figure 35), the oxidation level of the Ti coatings was increased with an increase in oxidation temperature. When the oxidation temperatures were 1073 and 1173 K, Ti coatings were completely oxidized to form  $\text{TiO}_2$  coatings when oxidation time became 40 h and 10 h, respectively. Figure 38 shows the cross-section SEM images of the coatings fabricated by the MCT and subsequent heat oxidation at 1273 K. Porous  $\text{TiO}_2$  coatings were obtained after just 3 h of oxidation.

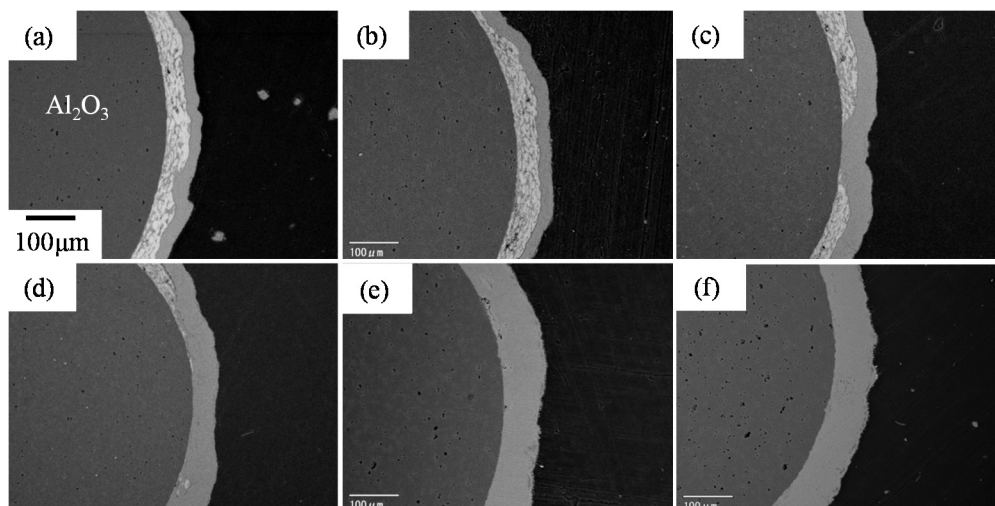


**Figure 36.** Cross-section SEM images of M10-1073 K-yh samples. (a) 10 h, (b) 15 h, (c) 20 h, (d) 30 h, (e) 40 h and (f) 50 h.

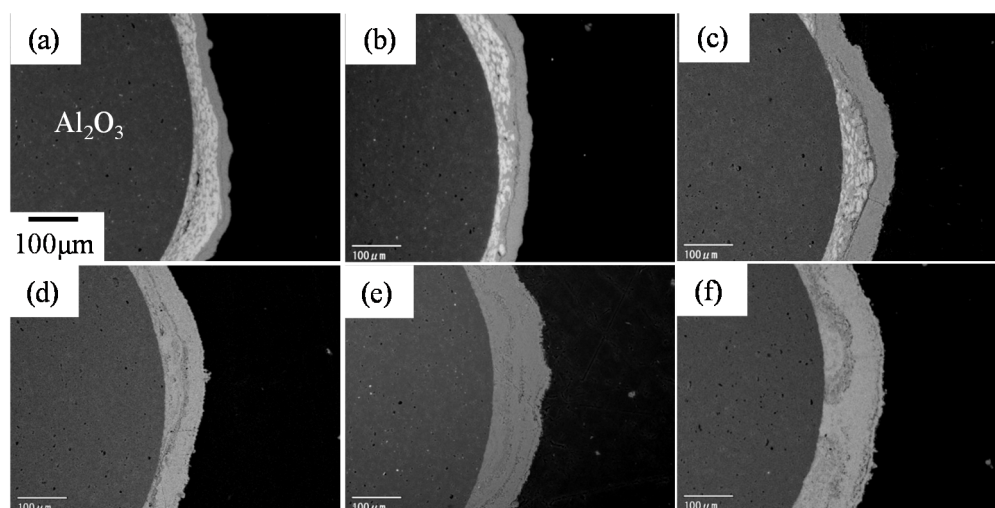


**Figure 37.** Cross-section SEM images of M10-1173 K-yh samples. (a) 0.5 h, (b) 1 h, (c) 3 h, (d) 10 h, (e) 30 h and (f) 50 h.

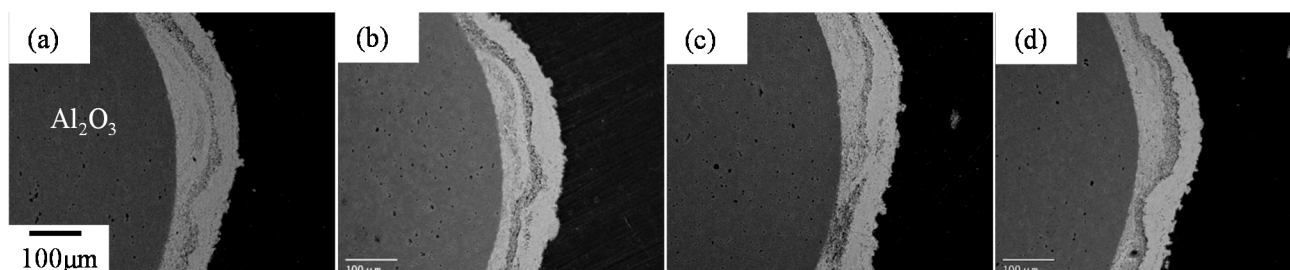


**Figure 38.** Cross-section SEM images of M10-1273 K-yh samples. (a) 3 h, (b) 10 h, (c) 30 h and (d) 50 h.

The change in concentration of MB solution (with the diameter of test cell is 18 mm) in the presence of the M10-xK-10h samples as a function of UV irradiation time is illustrated in Figure 39. The concentration of MB solution for the blank (marked with MB solution) hardly decreased, which means that the MB solution did not degrade under UV irradiation. In addition, Ti coatings have no photocatalytic

activity that appears as a marker with Ti coatings in Figure 39, which means that MB was not degraded under the action of Ti coatings and UV irradiation. However, the concentration of MB solution in the presence of the M10-xK-10h samples decreased to varying degrees. It indicates that the TiO<sub>2</sub> coatings and TiO<sub>2</sub>/Ti composite coatings showed photocatalytic activity toward MB solution.

Degradation rate constants calculated from plots of concentration *versus* irradiation time curves are presented in Figure 40. For the photocatalyst coatings of M10-xK-yh at 1073 K and 1173 K, *R* first increased and then decreased at an almost constant rate with extending oxidation time. With the photocatalyst coatings of sample at 1073 K and 1173 K, *R* first increased and then remained almost constant with extending oxidation time. The M10-1073 K-15h samples showed the highest photocatalytic activity.

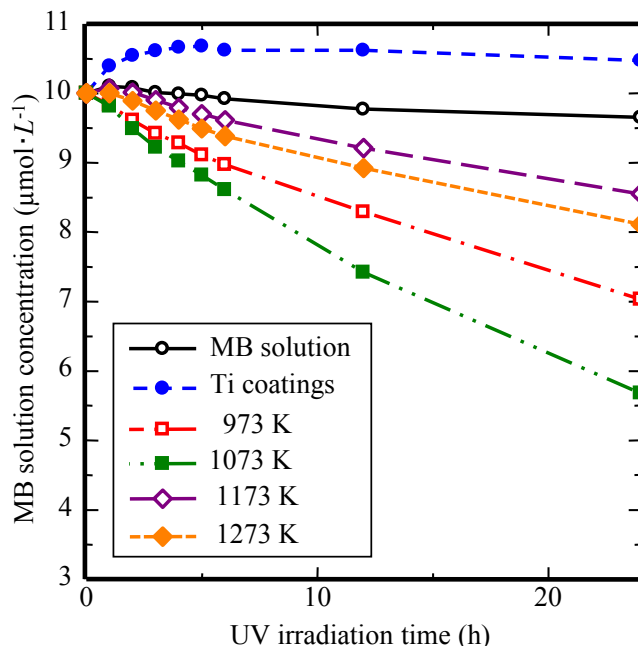


Figure 39. Degradation rate constant of M10-xK-yh samples.

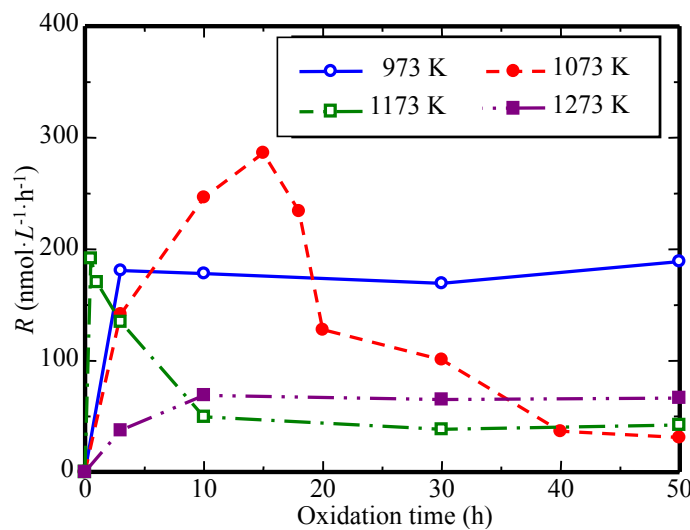


Figure 40. Relationship between dependence of degradation rate constants and the oxidation condition.

### 3.2. Influence on Photocatalyst Coatings of TiO<sub>2</sub> by Adding Metals

Additional information about the naming method of the prepared samples is provided as follows: “M10-*x*M” (M: Ni, Cr) indicates that the samples prepared with mixed Ti and M powder with *x* being the mass fraction of M by MCT at 480 rpm for 10 h. “M10-*x*M-*y*K/*z*h” are the final oxidized products of the “M10-*x*M”, and oxidation at the temperature of *y* K for *z* hour.

#### 3.2.1. Influence on Photocatalyst Coatings of TiO<sub>2</sub> by Adding Ni

Figure 41 shows the XRD patterns of the M10-*x*Ni coatings on Al<sub>2</sub>O<sub>3</sub> balls. Only diffraction peaks of Ti could be detected for the M10-Ti sample, which means the continuous Ti coatings were formed. For the Ti-5%Ni and Ti-10%Ni coatings, the diffraction peaks of alumina, Ti, and Ni were found, which means the Al<sub>2</sub>O<sub>3</sub> balls were coated by Ti and Ni coatings. However, the peaks of Ni could hardly be detected from the M10-1%Ni sample, indicating that the content of Ni in the coatings is rather small or even zero [52].

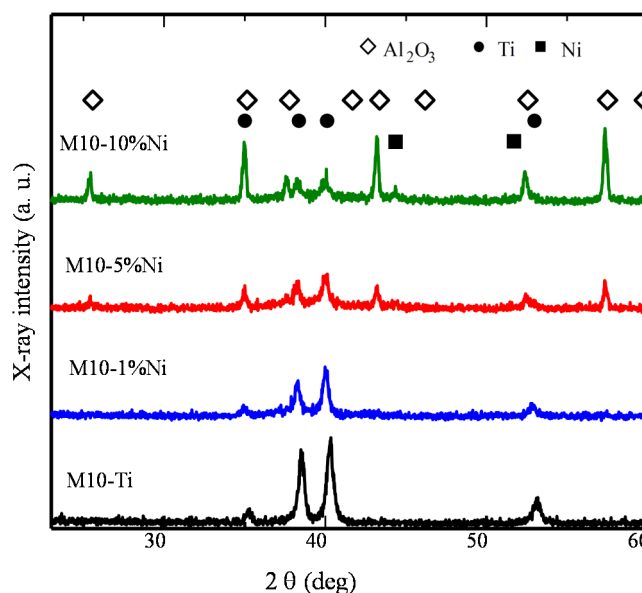


**Figure 41.** XRD patterns of M10-*x*Ni coatings samples.

The SEM images of surface microstructure of the M10-*x*Ni coatings on Al<sub>2</sub>O<sub>3</sub> balls prepared by MCT are shown as Figure 42. The areas of dark gray and light gray correspond to Ni particles and Ti particles, respectively. The Ni particles in the M10-*x*Ni coatings were rather few which means that the contents of Ni in the M10-*x*Ni coatings are rather small. In addition, the Ti-Ni coatings discontinued with the increase of Ni content.

Figure 43 shows the cross-section SEM images of the M10-*x*Ni coatings prepared by MCT. As pointed out above, the areas of dark gray and light gray correspond to Ni particles and Ti particles, respectively. The Ni particles are located in the inner layer of the M10-*x*Ni coatings. However, the thickness of coatings becomes thinner with increases in the content of Ni, which may relate to the bad wettability of Ni compared to Ti.

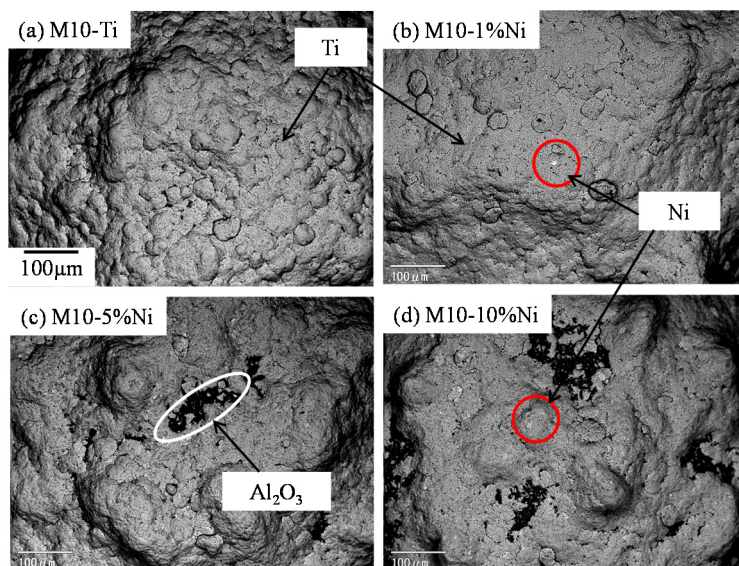


**Figure 42.** SEM images of surface structure of the M10-*x*Ni samples.

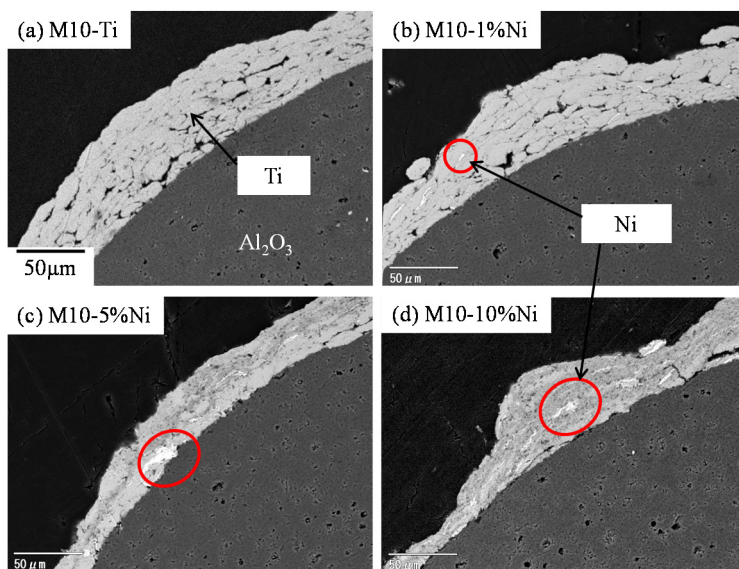


**Figure 43.** Cross-section SEM images of the M10-*x*Ni samples.

Figure 44 shows the XRD patterns of the M10-*x*Ni coatings after oxidation at elevated temperatures for 10 h. For Ti-1%Ni samples after oxidation (Figure 44a), only the diffraction peaks of rutile TiO<sub>2</sub> were detected. For Ti-5%Ni samples after oxidation (Figure 44b), besides rutile TiO<sub>2</sub>, the diffraction peaks of Al<sub>2</sub>O<sub>3</sub>, NiO and Ni<sub>2</sub>O<sub>3</sub> were also found (JCPDS card no. 89-7131 and 14-0841). It means that the Ni particles in the coatings were oxidized to form NiO and Ni<sub>2</sub>O<sub>3</sub>.

The cross-section SEM images of the M10-1%Ni-*x*K samples are shown as Figure 45. It can be seen that the thickness of TiO<sub>2</sub> has increased with increasing oxidation temperature. When the oxidation temperatures were 1173 K and 1273 K, the Ti coatings were totally oxidized to form TiO<sub>2</sub> coatings. Figure 46 shows the cross-section SEM images of the M10-5%Ni-*x*K samples. As the content of Ni in the coatings was rather small during MCT process, NiO and Ni<sub>2</sub>O<sub>3</sub> cannot be found in the SEM images after oxidation in air. The evolution of the coatings with 5% of Ni during oxidation is similar to that with 1% of Ni of Figure 45.

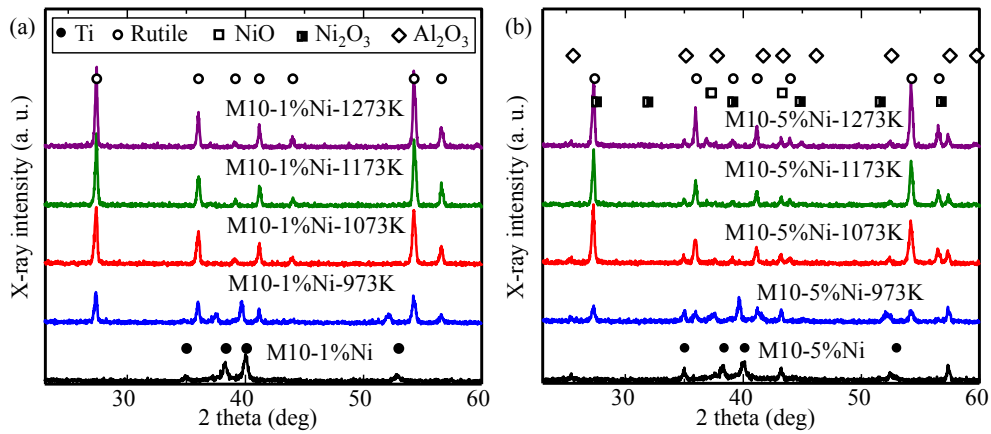


Figure 44. XRD patterns of M10-xNi coatings after oxidation.

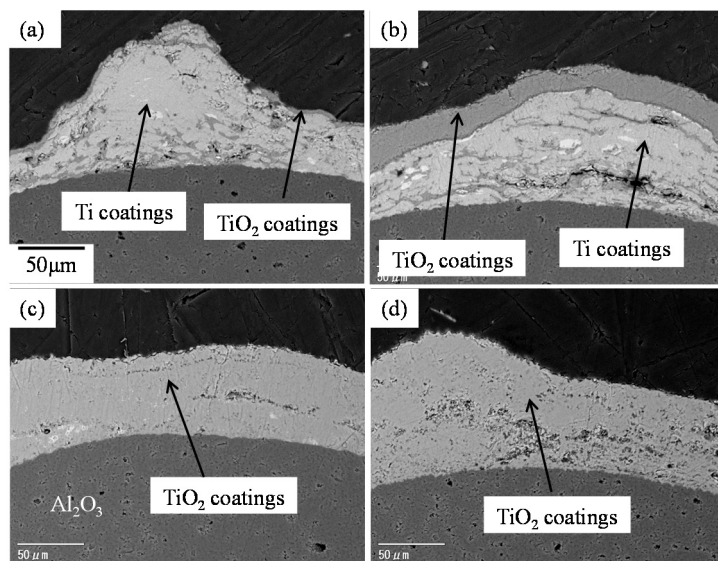


Figure 45. Cross-section SEM images of the M10-1%Ni-xK samples. (a) 973 K, (b) 1073 K, (c) 1173 K, (d) 1273 K.

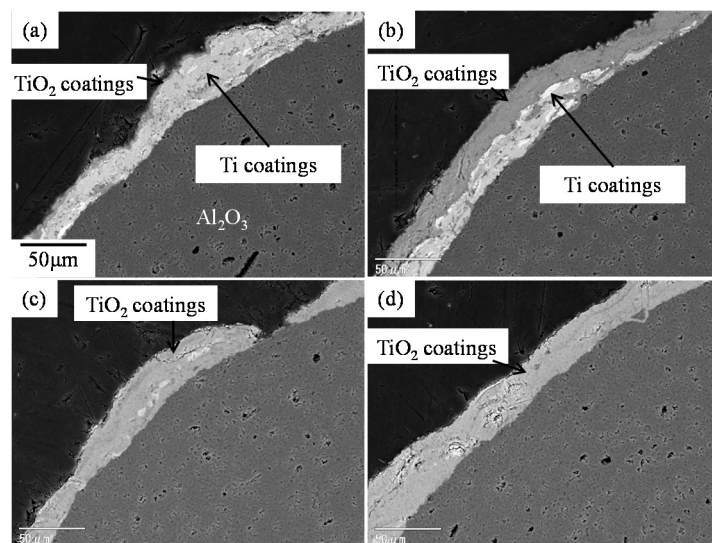
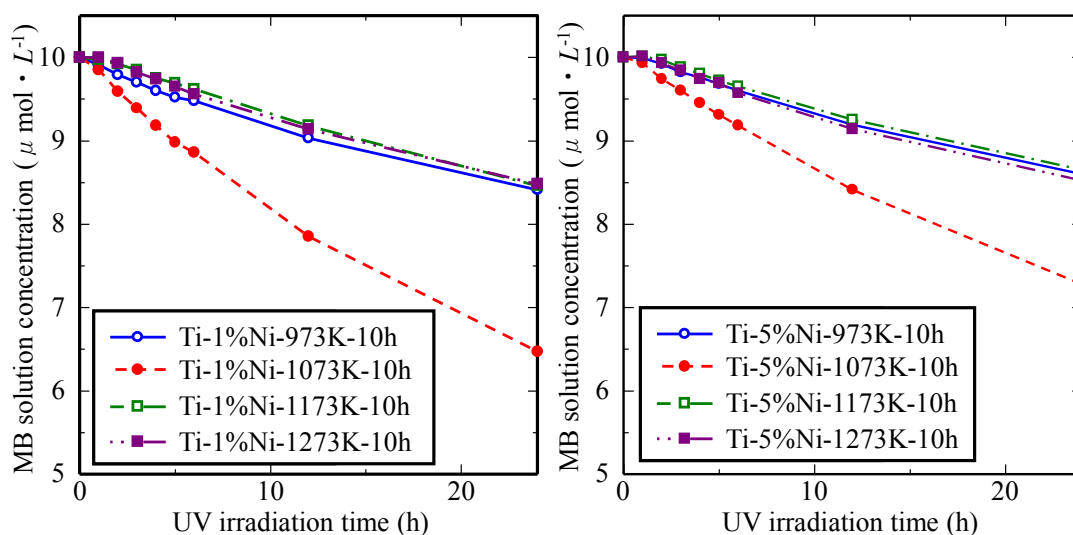


Figure 46. Cross-section SEM images of the M10-5%Ni-xK samples. (a) 973 K, (b) 1073 K, (c) 1173 K, (d) 1273 K.

The photocatalytic activity evaluation of the M10-*x*Ni-*y*K samples under UV was also performed, with a test cell diameter of 18 mm, shown as Figure 47. All the samples show photocatalytic activity, while MB solution hardly degrades by itself (Figure 39). MB solution with the M10-1%Ni-1073 K sample was degraded with a larger degradation content of MB solution than that of the M10-5%Ni-1073 K sample. For all the samples, MB solution with the sample oxidized at 1073 K was degraded with a larger degradation content of MB solution compared to the samples with other content of Ni. It is assumed that a p–n heterojunction may be formed, along with a corresponding inner electric field at the interface of TiO<sub>2</sub> and NiO. At equilibrium, the NiO region has a negative charge while the TiO<sub>2</sub> region has a positive charge. The electron-hole pairs at the surface of TiO<sub>2</sub> will be separated by the inner electric field. The holes move to the negative and the electrons flow to the positive field component. As a result, the recombination of photo-generated electron-hole pairs is decreased [53]. Thereby, the photocatalytic activity is enhanced.



**Figure 47.** MB degradation under UV of M10-*x*Ni-*y*K samples.

### 3.2.2. Influence on Photocatalyst Coatings of TiO<sub>2</sub> by Adding Cr

The M10-*x*Cr coatings show a metallic color, which is the same as M10-Ti [8]. In contrast, Figure 48 shows the M10-*x*Cr coatings after being oxidized at elevated temperatures for 15 h. The M10-*x*Cr-*y*K samples display various colors, which are grey, brown, and light-brown at 873 K, blue and light-yellow at 973 K, and light-white and light-grey at 1073 K. With added Cr, the color of samples obviously changes at each temperature. The color change of photocatalyst composite coatings hints that the samples with different thicknesses and nano-size crystal structures were formed by heat oxidation [35,54].

Figure 49 shows the XRD patterns of the samples. It can be seen that only the diffraction peaks of Ti are detected from the M10-Ti, and mixed-phase with anatase and rutile from the M10-*x*Cr-873 K. No characteristic peak of chromium oxide was found, which hints either doped Cr was incorporated in the crystalline of TiO<sub>2</sub>, or the chromium oxide was highly dispersed and its size was too small to be detected [55–57]. While at the temperature of 973 K, the phase obviously changes from anatase to rutile when adding Cr, which suggests that Cr could accelerate the phase transformation from anatase to rutile [58]. With temperatures up to 1073 K, it only appeared as a rutile phase. For comparison,  $X_R$  was

calculated from the respective peak intensities using Equation (2). The change of  $X_R$  is significant at each oxidation temperature and with different contents of Cr, especially at the temperature of 973 K, as shown in Figure 50.

The SEM images of M10- $x$ Cr- $y$ K samples are shown in Figure 51, compared with the temperature and adding Cr. With increases in the temperature, the crystals increase in number and grow to form a nano-size structure, from Figure 51a,c,e, which is similar to Figure 25. While adding Cr, the microstructure of samples at each oxidation temperature becomes larger, from Figure 51b,d,f. The effect of adding Cr on the surface microstructure is significant. Considering the changes of surface microstructure and phase transformation, the conclusion could be drawn that the phase transformation from anatase to rutile had been affected by the crystal size [21,59].

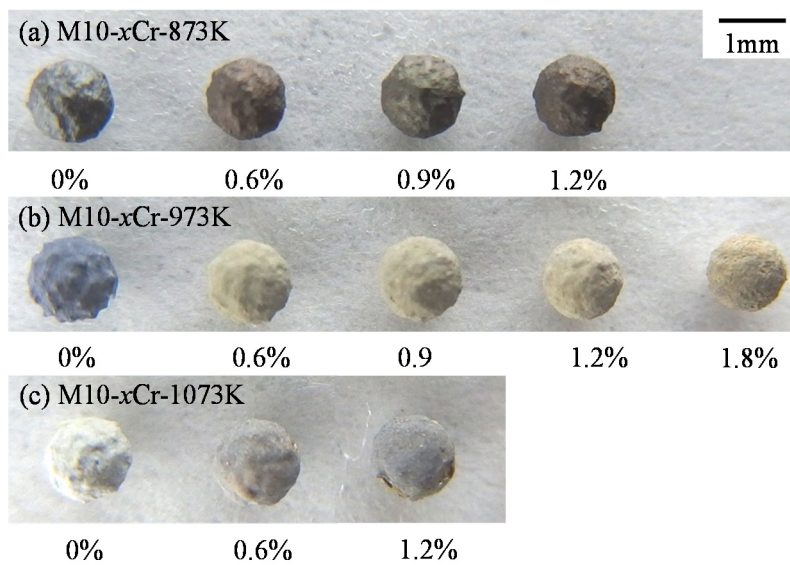


Figure 48. Photograph of the samples.

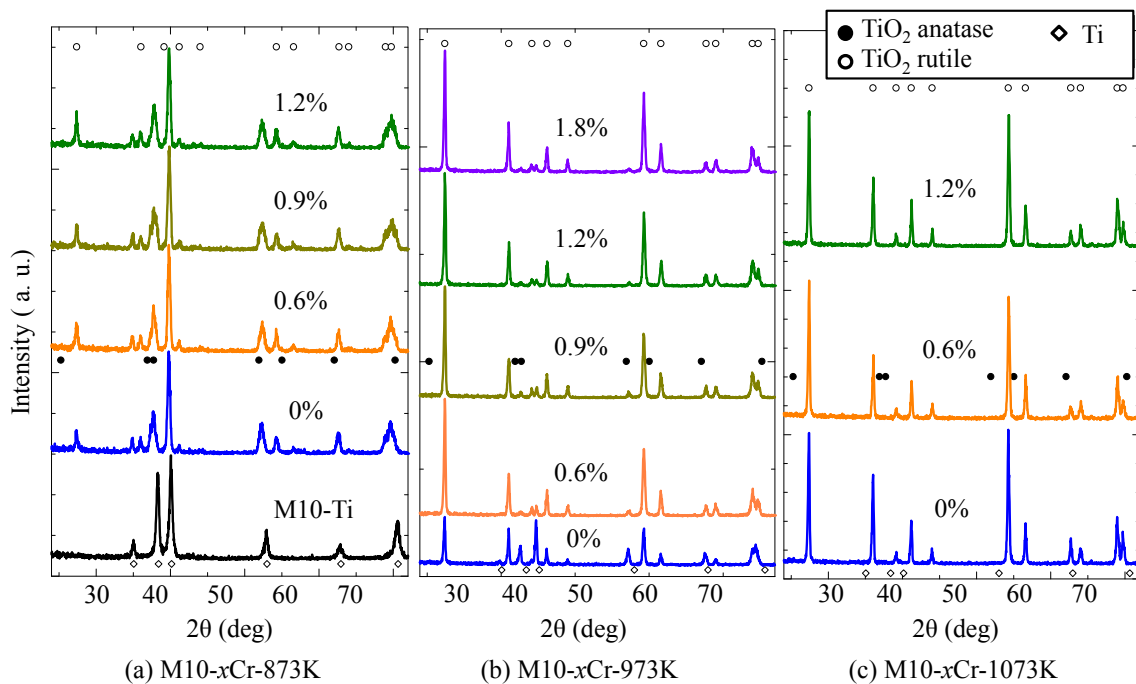
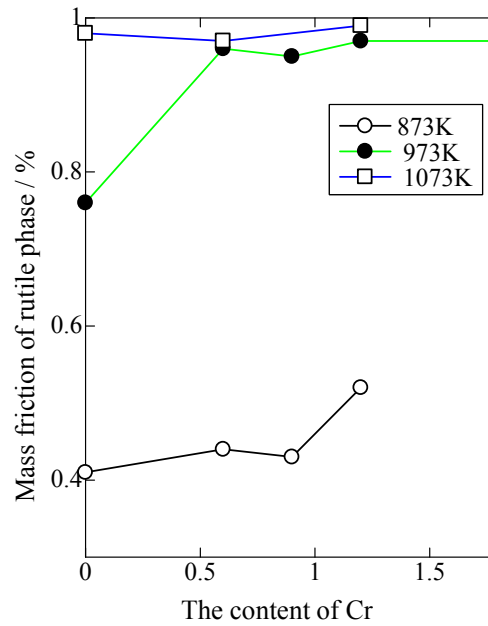
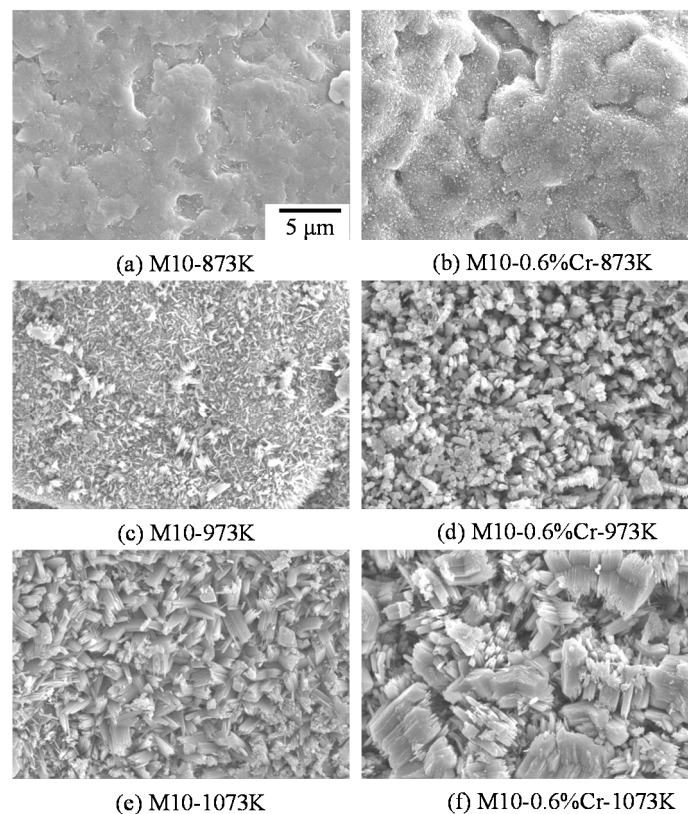


Figure 49. XRD patterns of the M10- $x$ Cr- $y$ K samples.

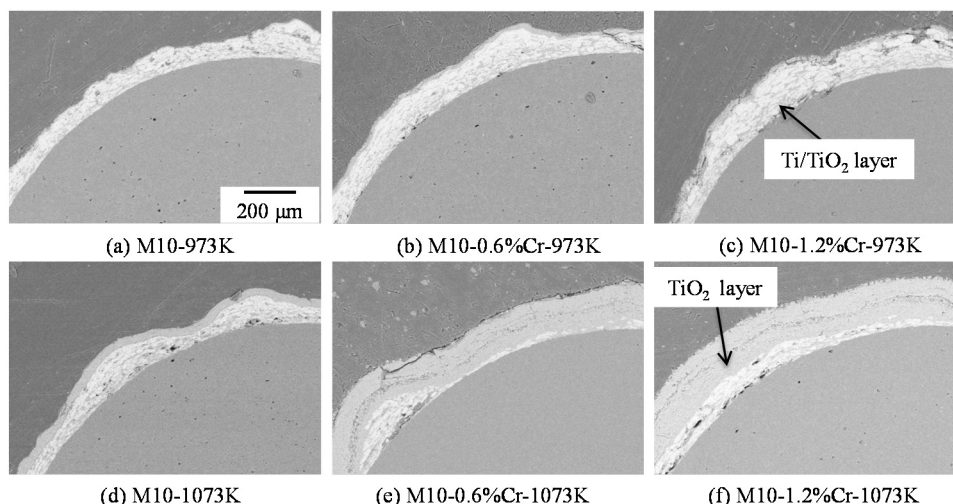


**Figure 50.** The change of  $X_R$  with the content of Cr.



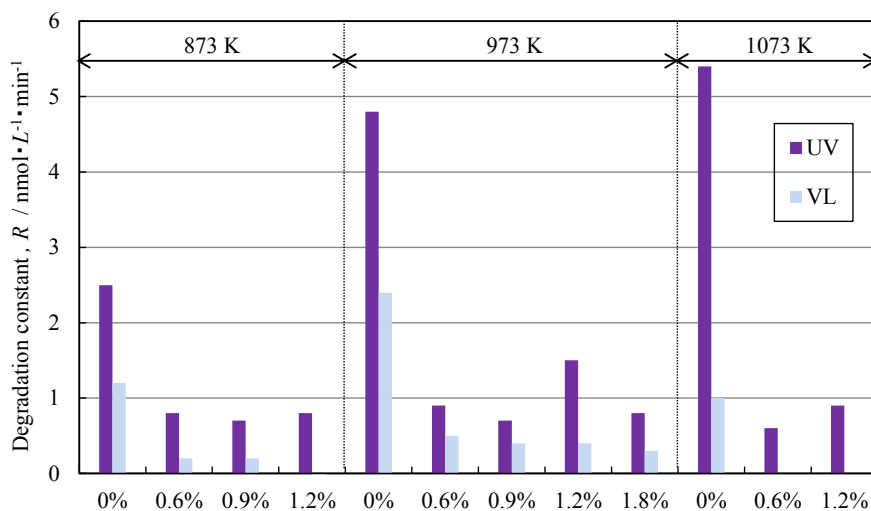
**Figure 51.** SEM images of surfaces of M10-xCr-yK samples.

Figure 52 shows the cross section of M10-xCr-yK samples. The oxidized layer cannot be detected from the samples at the temperature of 873 K. At the temperature of 973 K, a thin oxidized layer could be found from M10-973 K, while adding Cr, the layer thickens. At 1073 K, the growth of layer is more obvious, when adding Cr. The change hints that the presence of Cr could significantly accelerate the growth of the oxidized layer, which is similar to the effect on surface microstructure.



**Figure 52.** SEM images of cross sections of M10-*x*Cr-*y*K samples.

The photocatalytic activity of the samples had been investigated by degradation of MB solution under UV and visible light, when the diameter of the test cell is 40 mm, shown as Figure 53. With the addition of Cr, the photocatalytic activity under UV and visible light is relatively higher at 973 K, which might be caused by the nano-size microstructure and/or the recombination site from the excess Cr. The overall trends of photocatalytic activity was that of decrease, when adding Cr at each temperature. It shows that photocatalytic activities were affected by the surface morphology and crystal structure.



**Figure 53.** Degradation rate constant and  $X_R$  of M10-*x*Cr-*y*K samples.

### 3.3. Influence on Photocatalyst Coatings of TiO<sub>2</sub> by Molten Salt Treatment

Firstly, additional information about the naming method of prepared samples is provided as follows: The Ti coatings will be treated by molten salt treatment of KNO<sub>3</sub> (99.0%, 167-04045, Wako Pure Chemical Industries, Ltd., Chuo-ku, Japan) under the temperature of *x* K for 3 h, named as K-*x*. For comparison, the samples will be oxidized at the temperature of *y* K for 3 h, named as H-*y*.

The appearance photograph of Ti coatings treated by molten salt treatment and oxidation process is shown as Figure 54. The K-*x* samples treated by molten salt treatment display various colors, yellow at

673 K, blue at 773 K, dark-purple at 873 K, shown in Figure 54a. While the H-y samples treated by oxidation process are similar but a little lighter than that of the K-x samples, shown in Figure 54b. The color of TiO<sub>2</sub> is related to the thickness of TiO<sub>2</sub> coatings, and the presence of potassium affected the TiO<sub>2</sub> coatings [28,37,60].

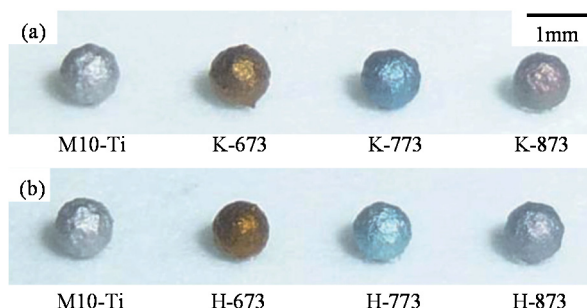


**Figure 54.** Photograph of the samples.

Figure 55 shows the XRD patterns of the samples. It can be seen that only the diffraction peaks of Ti are detected from the M10-Ti, and anatase phase near 38° and 52° from the treated samples of K-x and H-y. Compared with these two treatments, the XRD patterns show very little change, which hints that the content of potassium is too little to have an obvious effect on the phase transformation. In order to compare the influence of molten salt treatment, the content of potassium in the K-x samples had been investigated by EDS, as shown in Table 4.

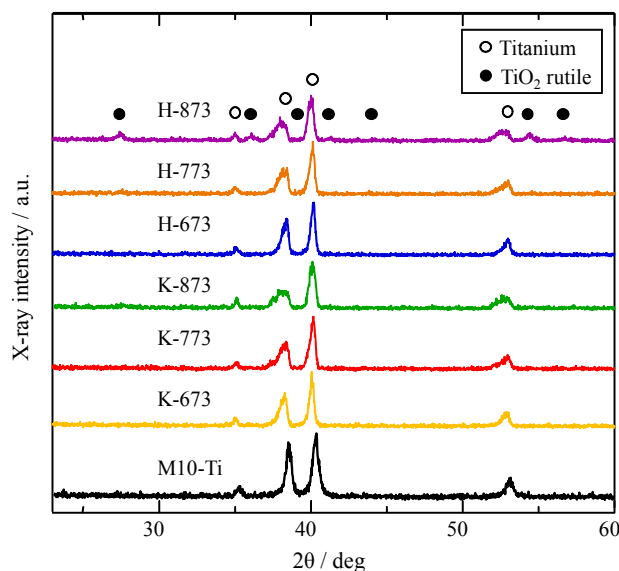


**Figure 55.** XRD patterns of the samples.

**Table 4.** Composition of the specimens by molten salt treatment.

Element	Titanium	Oxygen	Potassium
M10-Ti	94.5	5.5	0.0
K-673	86.4	13.6	0.0
K-773	72.8	26.5	0.7
K-873	58.5	39.5	2.0

The SEM images of surfaces microstructure of samples treated by molten salt treatment and an oxidation process are shown in Figure 56, compared with the temperature and treatment method. The nano-size structure could be detected by oxidation process from Figure 56a,b,c, until the temperature reaches 873 K, which is considered to be anatase phase, according to the XRD result. Meanwhile, the nano-size structure could be detected by molten salt treatment from Figure 56d,e,f, and the structure grew larger. Therefore, the structure formed at 673 K and 773 K by molten salt treatment may be related to amorphous potassium titanate [60].

The photocatalytic activity of the samples had been investigated by degradation of MB solution under UV and visible light, shown as Figure 57. The photocatalytic activity of the K-x samples under UV is a little higher than that of the H-y samples, while the photocatalytic activity of the K-x samples under visible light had been significantly enhanced. It might be related with the nano-size microstructure and/or amorphous phase caused by the presence of potassium, which is considered to provide good absorption [61].

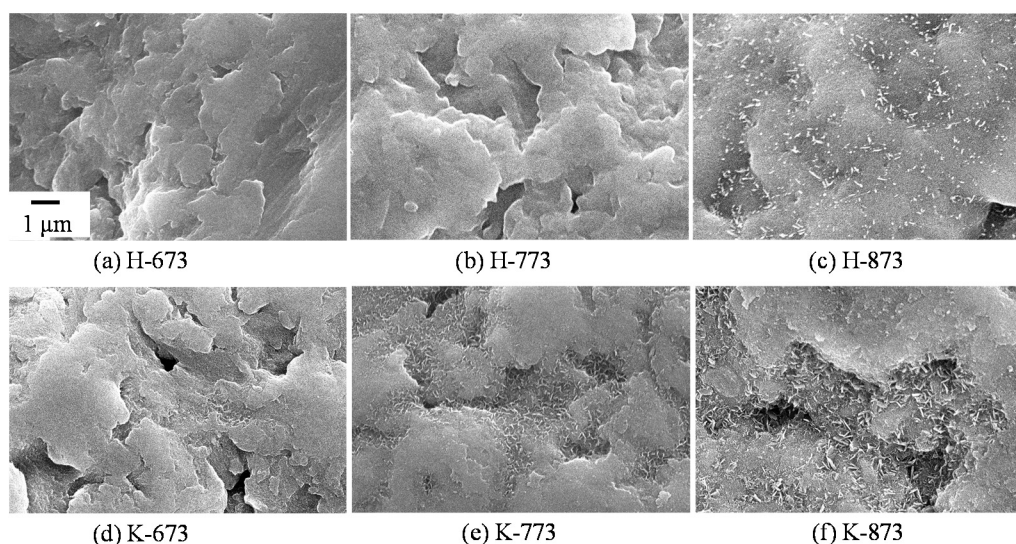


**Figure 56.** SEM micrographs of surfaces microstructure of the K-x and H-y samples.

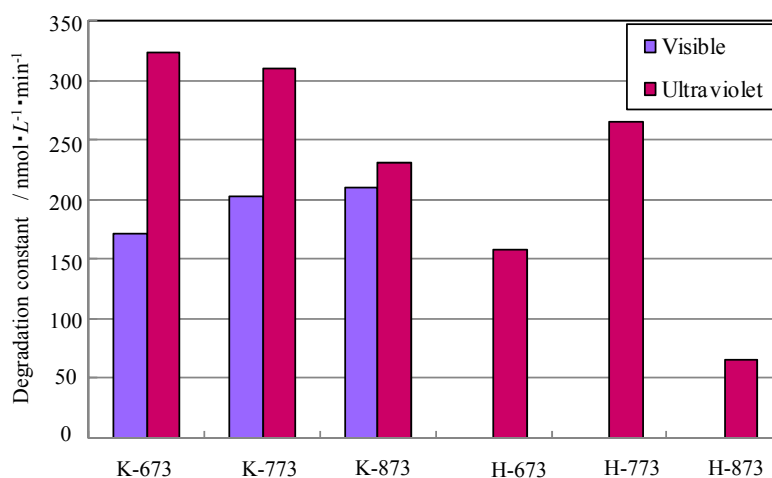


**Figure 57.** Degradation rate constant of the samples.

#### 4. Conclusions

This review presents the latest results of studies directed at photocatalyst coatings of TiO<sub>2</sub> prepared using the mechanical coating technique (MCT) and its application.

MCT as a novel formation process is affected by the electronegativity and plastic deformability of the metal, MCT speed and time. The formation process of the metal coatings in MCT is considered to consist of four stages: the nucleation by adhesion, the formation and coalescence of discrete islands, formation and thickening of continuous coatings, and exfoliation of continuous coatings. Further, based on the MCT concept for preparing composite coatings on alumina balls, a two-step MCT was developed to fabricate the composite photocatalyst coatings. Compared with traditional coating techniques (requiring large and complicated equipment, vacuum conditions, having high fabrication cost, difficulties in forming on spherical substrates), MCT is a simple, low cost and useful coating formation process, which could be used to fabricate photocatalyst coatings.

On the other hand, this review discusses the influence on the fabrication of photocatalyst coatings after MCT and improvement of the photocatalytic activity: oxidation conditions, coating materials, and melt salt treatment. The oxidation conditions could significantly affect the crystal phase and surface structure, and the photocatalyst coatings showed the highest photocatalytic activity with the oxidation condition of 1073 K for 15 h. The photocatalyst coatings had been fabricated using composite metal powder, and the surface structure and photocatalytic activity also had been affected by different metal powders (Ni, Cr). The Ni powder could enhance the photocatalytic activity under oxidation at 1073 K, while Cr powder had difficulty in enhancing the photocatalytic activity with a relatively high content of Cr powder. The melt salt treatment with KNO<sub>3</sub> is an effective method to form a nano-size structure and enhance photocatalytic activity.

#### Conflicts of Interest

The authors declare no conflict of interest.

#### References

1. Ohring, M. *Materials Science of Thin Films*; Academic Press: New York, NY, USA, 2001.
2. Freund, L.B.; Suresh, S. *Thin Film Materials-stress, Defect Formation and Surface Evolution*; Cambridge University Press: Cambridge, UK, 2004.
3. Lu, Y.; Hao, L.; Yoshida, H. Chapter12: Mechanical coating technique for composite films and composite photocatalyst films. In *Composite and Their Applications*; Hu, N., Ed.; Intech Press: Rigeika, Croatia, 2012.
4. Mattox, D.M. *Handbook of Physical Vapor Deposition (PVD) Processing*; William Andrew: Burlington, VT, USA, 2010.
5. Pierson, H.O. *Handbook of Chemical Vapor Deposition-Principles, Technology and Application*; William Andrew Publishing: New York, NY, USA, 1999.
6. Wasa, K.; Kitabatake, M.; Adachi, H. *Thin Film Materials Technology: Sputtering of Compound Materials*; William Andrew Publishing: New York, NY, USA, 2003.

7. Yoshida, H.; Lu, Y.; Hirohashi, M. Fabrication of metallic titanium film by mechanical coating technique. In Proceedings of the 5th International Forum on Advanced Material Science and Technology (IFAMST 5), Zhangjiajie, China, 11 June 2006.
8. Yoshida, H.; Lu, Y.; Nakayama, H.; Hirohashi, M. Fabrication of TiO<sub>2</sub> film by mechanical coating technique and its photocatalytic activity. *J. Alloys Compd.* **2009**, *475*, 383–386.
9. Dozzi, M.V.; Selli, E. Doping TiO<sub>2</sub> with p-block elements: Effects on photocatalytic activity. *J. Photochim. Photobiol. C* **2013**, *14*, 13–28.
10. Kumar, S.G.; Devi, L.G. Review on modified TiO<sub>2</sub> photocatalysis under UV/visible light: Selected results and related mechanisms on interfacial charge carrier transfer dynamics. *J. Phys. Chem. A* **2011**, *115*, 13211–13241.
11. Nakata, K.; Fujishima, A. TiO<sub>2</sub> photocatalysis: Design and applications. *J. Photochim. Photobiol. C* **2012**, *13*, 169–189.
12. Liu, M.; Qiu, X.; Hashimoto, K.; Miyauchi, M. Cu (II) oxide amorphous nanoclusters grafted Ti<sup>3+</sup> self-doped TiO<sub>2</sub>: An efficient visible light photocatalyst. *J. Mater. Chem. A* **2014**, *2*, 13571–13579.
13. Gratzel, M. Photoelectrochemical cells. *Nature* **2001**, *238*, 338–344.
14. Zhang, S. The microscopic origin of the doping limits in semiconductors and wide-gap materials and recent developments in overcoming these limits: A review. *J. Phys. Condens. Mat.* **2002**, *14*, doi:10.1088/0953-8984/14/34/201.
15. Chen, S.; Chen, L.; Gao, S.; Cao, G. The preparation of coupled SnO<sub>2</sub>/TiO<sub>2</sub> photocatalyst by ball milling. *Mater. Chem. Phys.* **2006**, *98*, 116–120.
16. Pan, L.; Zou, J.; Zhang, X.; Wang, L. Photoisomerization of norbornadiene to quadricyclane using transition metal doped TiO<sub>2</sub>. *Ind. Eng. Chem. Res.* **2010**, *49*, 8526–8531.
17. Gai, Y.; Li, J.; Li, S.; Xia, J.; Wei, S. Design of narrow-gap TiO<sub>2</sub> for enhanced photoelectrochemical activity: A passivated codoping approach. *Phys. Rev. Lett.* **2009**, *102*, doi: 10.1103/PhysRevLett.102.036402.
18. Yan, M.; Chen, F.; Zhang, J.; Anpo, M. Preparation of controllable crystalline titania and study on the photocatalytic properties. *J. Phys. Chem. B* **2005**, *109*, 8673–8678.
19. He, Z.; Cai, Q.; Fang, H.; Situ, G.; Qiu, J.; Song, S.; Chen, J. Photocatalytic activity of TiO<sub>2</sub> containing anatase nanoparticles and rutile nanoflower structure consisting of nanorods. *J. Environ. Sci.* **2013**, *25*, 2460–2468.
20. Liu, J.; Yu, X.; Liu, Q.; Liu, R.; Shang, X.; Zhang, S.; Li, W.; Zheng, W.; Zhang, G.; Cao, H.; *et al.* Surface-phase junctions of branched TiO<sub>2</sub> nanorod arrays for efficient photoelectrochemical water splitting. *Appl. Catal. B* **2014**, *158–159*, 296–300.
21. Zhang, J.; Xu, Q.; Feng, Z.; Li, M.; Li, C. Importance of the relationship between surface phases and photocatalytic activity of TiO<sub>2</sub>. *Angew. Chem. Int. Ed.* **2008**, *47*, 1766–1769.
22. Lu, Y.; Yoshida, H.; Nakayama, H.; Hao, L.; Hirohashi, M. Formation of TiO<sub>2</sub>/Ti composite photocatalyst film by 2-step mechanical coating technique. *Mater. Sci. Forum* **2011**, *675–677*, 1229–1232.
23. Lu, Y.; Hao, L.; Toh, K.; Yoshida, H. Fabrication of TiO<sub>2</sub>-Cu composite photocatalyst thin film by twostep mechanical coating technique and its photocatalytic activity. *Adv. Mater. Res.* **2012**, *415–417*, 1942–1948.

24. Hao, L.; Lu, Y.; Asanuma, H.; Guo, J. The influence of the processing parameters on the formation of iron thin films on alumina balls by mechanical coating technique. *J. Mater. Proc. Technol.* **2012**, *212*, 1169–1176.
25. Hao, L.; Lu, Y.; Sato, H.; Asanuma, H.; Guo, J. Fabrication of zinc coatings on alumina balls from zinc powder by mechanical coating technique and the process analysis. *Powder Technol.* **2012**, *228*, 377–384.
26. Lu, Y.; Matsuzaka, K.; Hao, L.; Hirakawa, Y.; Yoshida, H.; Pan, F.S. Photocatalytic activity of TiO<sub>2</sub>/Ti composite coatings fabricated by mechanical coating technique and subsequent heat oxidation. *Mater. Sci. Semicon. Process.* **2013**, *16*, 1949–1956.
27. Lu, Y.; Kobayashi, K.; Guan, S.; Hao, L.; Yoshida, H.; Asanuma, H.; Chen, J. Influence of oxidation process on photocatalytic activity of photocatalyst coatings by mechanical coating technique. *Mater. Sci. Semicon. Process.* **2015**, *30*, 128–134.
28. Hirakawa, Y.; Lu, Y.; Yoshida, H.; Matsuzaka, K.; Hao, L.; Sato, H. Fabrication and evaluation of visible light active TiO<sub>2</sub> photocatalyst by molten salt method. *J. Jpn. Inst. Met. Mater.* **2013**, *77*, 287–293.
29. Takaya, S.; Lu, Y.; Guan, S.; Miyazawa, K.; Yoshida, H.; Asanuma, H. Fabrication of the photocatalyst thin films of nano-structured potassium titanate by molten salt treatment and its photocatalytic activity. *Surf. Coat. Technol.* **2015**, *275*, 260–263.
30. Suryanarayana, C. Mechanical alloying and milling. *Prog. Mater. Sci.* **2001**, *46*, 1–184.
31. Kotz, J.C.; Treichel, P.M.; Townsend, J. *Chemistry & Chemical Reactivity*, 8th ed.; Mary Finch: Belmont, OH, USA, 2011.
32. John, A. *Dean: Lange's Handbook of Chemistry*, 14th ed.; McGraw-Hill: New York, NY, USA, 1999; Volume 29.
33. Allen, L.C. Electronegativity is the average one-electron energy of the valence-shell electrons in ground-state free atoms. *J. Am. Chem. Soc.* **1989**, *111*, 9003–9014.
34. Howatson, A.M.; Lund, P.G.; Todd, J.D. *Engineering Tables and Data*; Chapman & Hall: London, UK, 1991.
35. Hao, L.; Lu, Y.; Sato, H.; Asanuma, H.; Guo, J. Analysis on energy transfer during mechanical coating and ball milling—Supported by electric power measurement in planetary ball mill. *Int. J. Miner. Process.* **2013**, *121*, 51.
36. The Japan Titanium Society. *Processing Technology of Titanium*; Nikkan Kogyo Shimbun: Tokyo, Japan, 1992.
37. Zhang, X.; Lei, L. One step preparation of visible-light responsive Fe–TiO<sub>2</sub> coating photocatalysts by MOCVD. *Mater. Lett.* **2008**, *62*, 895–897.
38. Spuur, R.A.; Myers, H. Quantitative analysis of anatase-rutile mixtures with an X-ray diffractometer. *Anal. Chem.* **1957**, *29*, 760–762.
39. Kakiuchi, K.; Hosono, E.; Imai, H.; Kimura, T.; Fujihara, S. {111}-faceting of low-temperature processed rutile TiO<sub>2</sub> rods. *J. Cryst. Growth* **2006**, *293*, 541–545.
40. Ferry, J.D. *Viscoelastic Properties of Polymers*; Wiley: New York, NY, USA, 1980.
41. Luttrell, T.; Halpegamage, S.; Tao, J.; Kramer, A.; Sutter, E.; Batzill, M. Why is anatase a better photocatalyst than rutile? Model studies on epitaxial TiO<sub>2</sub> films. *Sci. Rep.* **2014**, *4*, 1–8.

42. Liu, X.; Zhang, H.; Liu, C.; Chen, J.; Li, G.; An, T. Wong, P.; Zhao, H. UV and visible light photoelectrocatalytic bactericidal performance of 100% {111}-faceted rutile TiO<sub>2</sub> photoanode. *Catal. Today* **2014**, *224*, 77–82.
43. Hurum, D.; Agrios, A.; Gray, K.; Rajh, T.; Thurnauer, M. Explaining the enhanced photocatalytic activity of degussa P25 mixed-phase TiO<sub>2</sub> using EPR. *J. Phys. Chem. B* **2003**, *107*, 4545–4549.
44. Liu, B.; Aydil, E. Growth of oriented single-crystalline rutile TiO<sub>2</sub> nanorodson transparent conducting substrates for dye-sensitized solar cells. *J. Am. Chem. Soc.* **2009**, *131*, 3985–3990.
45. Ozawa, K.; Emori, M.; Yamamoto, S.; Yukawa, R.; Yamamoto, S.; Hobara, R.; Fujikawa, K.; Sakama, H.; Matsuda, I. Electron-hole recombination time at TiO<sub>2</sub> single-crystal surfaces: Influence of surface band bending. *J. Phys. Chem. Lett.* **2014**, *5*, 1953–1957.
46. Chen, X.; Shen, S.; Guo, L.; Mao, S. Semiconductor-based photocatalytic hydrogen generation. *Chem. Rev.* **2010**, *110*, 6503–6570.
47. Chen, X.; Wang, X.; Hou, Y.; Huang, J.; Wu, L.; Fu, X. The effect of postnitridation annealing on the surface property and photocatalytic performance of N-doped TiO<sub>2</sub> under visible light irradiation. *J. Catal.* **2008**, *255*, 59–67.
48. Asahi, R.; Morikawa, T.; Ohwaki, T.; Aoki, K.; Taga, Y. Visible-light photocatalysis in nitrogen-doped titanium oxides. *Science* **2001**, *293*, 269–271.
49. Sheng, J.; Hu, L.H.; Li, W.X.; Mo, L.E.; Tian, H.J.; Dai, S.Y. Formation of single-crystalline rutile TiO<sub>2</sub> splitting microspheres for dye-sensitized solar cells. *Sol. Energy* **2011**, *85*, 2697–2703.
50. Bae, E.; Murakami, N.; Nakamura, M.; Ohno, T. Effect of chemical etching by sulfuric acid or H<sub>2</sub>O<sub>2</sub>-NH<sub>3</sub> mixed solution on the photocatalytic activity of rutile TiO<sub>2</sub> nanorods. *Appl. Catal. A* **2010**, *380*, 48–54.
51. Li, C.J.; Xu, G.R.; Zhang, B.H.; Gong, J.R. High selectivity in visible-light-driven partial photocatalytic oxidation of benzyl alcohol into benzaldehyde over single-crystalline rutile TiO<sub>2</sub> nanorods. *Appl. Catal. B* **2012**, *115–116*, 201–208.
52. Lu, Y.; Hao, L.; Matsuzaka, K.; Yoshida, H.; Asanuma, H.; Chen, J.; Pan, F. Titanium dioxide-nickel oxide composite coatings: Preparation by mechanical coating/thermal oxidation and photocatalytic activity. *Mater. Sci. Semicon. Process.* **2014**, *24*, 138–145.
53. Guan, S.; Lu, Y.; Hao, L.; Takaya, S.; Miyazawa, K.; Yoshida, H.; Asanuma, H. Influence of oxidation conditions on photocatalytic activity of Cr-TiO<sub>2</sub> coatings by mechanical coating technique. In Proceedings of the 9th International Forum on Advanced Material Science and Technology (IFAMST 9), Xiamen, China, 1 December 2014.
54. Chen, S.; Zhang, S.; Liu, W.; Zhao, W. Preparation and activity evaluation of p-n junction photocatalyst NiO/TiO<sub>2</sub>. *J. Hazard. Mater.* **2008**, *155*, 320–326.
55. Pan, C.; Wu, J. Visible-light response Cr-doped TiO<sub>2-x</sub> NX photocatalysts. *Mater. Chem. Phys.* **2006**, *100*, 102–107.
56. Zhu, J.; Deng, Z.; Chen, F.; Zhang, J.; Chen, H.; Anpo, M.; Huang, J.; Zhang, L. Hydrothermal doping method for preparation of Cr<sup>3+</sup>-TiO<sub>2</sub> photocatalysts with concentration gradient distribution of Cr<sup>3+</sup>. *Appl. Catal. B* **2006**, *62*, 329–335.
57. Peng, Y.; Huang, G.; Huang, W. Visible-light absorption and photocatalytic activity of Cr-doped TiO<sub>2</sub> nanocrystal films. *Adv. Powder Technol.* **2012**, *23*, 8–12.

58. Hajjaji, A.; Gaidi, M.; Bessais, B.; Khakani, M. Effect of Cr incorporation on the structural and optoelectronic properties of TiO<sub>2</sub>:Cr deposited by means of a magnetron co-sputtering process. *Appl. Surf. Sci.* **2011**, *257*, 10351–10357.
59. Tretyachenko, E.; Gorokhovskiy, A.; Yurkov, G.; Fedorov, F.; Vikulova, M.; Kovaleva, D.; Orozaliev, E. Adsorption and photo-catalytic properties of layered lepidocrocite-like quasi-amorphous compounds based on modified potassium polytitanates. *Particuology* **2014**, *17*, 22–28.
60. Gorokhovskiy, A.V.; Escalante-Garcia, J.I.; Sanchez-Monjaras, T.; Gutierrez-Chavarria, C.A. Synthesis of potassium polytitanate precursors by treatment of TiO<sub>2</sub> with molten mixtures of KNO<sub>3</sub> and KOH. *J. Eur. Ceram. Soc.* **2004**, *24*, 3541–3546.
61. Masaki, N.; Uchida, S.; Yamane, H.; Sato, T. Hydrothermal synthesis of potassium titanates in Ti-KOH-H<sub>2</sub>O system. *J. Mater. Sci.* **2000**, *35*, 3307–3311.

© 2015 by the authors; licensee MDPI, Basel, Switzerland. This article is an open access article distributed under the terms and conditions of the Creative Commons Attribution license (<http://creativecommons.org/licenses/by/4.0/>).